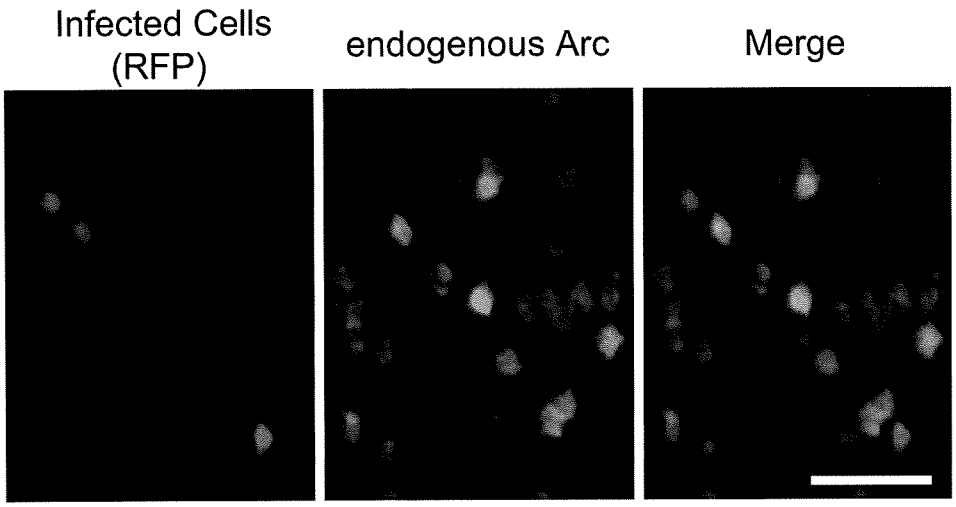

Fig. S6. Expression of endogenous *Arc/Arg-3.1* in virus-infected neurons in the visual cortex. A majority of reporter-virus-infected neurons expressed increased levels of endogenous *Arc/Arg-3.1* in the activated visual cortex. (Scale bar, 50 μm.)

Cellular/Molecular

Control of Cortical Axon Elongation by a GABA-Driven Ca^{2+}/Calmodulin-Dependent Protein Kinase Cascade

Natsumi Ageta-Ishihara,[1] Sayaka Takemoto-Kimura,[1] Mio Nonaka,[1] Aki Adachi-Morishima,[1] Kanzo Suzuki,[1] Satoshi Kamijo,[1] Hajime Fujii,[1] Tatsuo Mano,[1] Frank Blaeser,[2] Talal A. Chatila,[3] Hidenobu Mizuno,[4,5] Tomoo Hirano,[4,5] Yoshiaki Tagawa,[4,5] Hiroyuki Okuno,[1,5] and Haruhiko Bito[1,5]

[1]Department of Neurochemistry, Graduate School of Medicine, University of Tokyo, Tokyo 113-0033, Japan, [2]Institute of Transfusion Medicine, University Hospital Leipzig, 04129 Leipzig, Germany, [3]Division of Immunology, Allergy, and Rheumatology, Department of Pediatrics, David Geffen School of Medicine, University of California, Los Angeles, Los Angeles, California 90095-1752, [4]Department of Biophysics, Kyoto University Graduate School of Science, Kyoto 606-8502, Japan, and [5]Core Research for Evolutional Science and Technology, Japan Science and Technology Agency, Saitama 332-0012, Japan

Ca^{2+} signaling plays important roles during both axonal and dendritic growth. Yet whether and how Ca^{2+} rises may trigger and contribute to the development of long-range cortical connections remains mostly unknown. Here, we demonstrate that two separate limbs of the Ca^{2+}/calmodulin-dependent protein kinase kinase (CaMKK)–CaMKI cascades, CaMKK–CaMKIα and CaMKK–CaMKIγ, critically coordinate axonal and dendritic morphogenesis of cortical neurons, respectively. The axon-specific morphological phenotype required a diffuse cytoplasmic localization and a strikingly α-isoform-specific kinase activity of CaMKI. Unexpectedly, treatment with muscimol, a $GABA_A$ receptor agonist, selectively stimulated elongation of axons but not of dendrites, and the CaMKK–CaMKIα cascade critically mediated this axonogenic effect. Consistent with these findings, during early brain development, *in vivo* knockdown of CaMKIα significantly impaired the terminal axonal extension and thereby perturbed the refinement of the interhemispheric callosal projections into the contralateral cortices. Our findings thus indicate a novel role for the GABA-driven CaMKK–CaMKIα cascade as a mechanism critical for accurate cortical axon pathfinding, an essential process that may contribute to fine-tuning the formation of interhemispheric connectivity during the perinatal development of the CNS.

Introduction

The formation of cortical neural circuits requires precisely controlled development of axons and dendrites. Although the molecular mechanisms underlying axon guidance in the CNS have been intensively studied (Tessier-Lavigne and Goodman, 1996; Dickson, 2002), the intracellular signaling and cytoskeletal remodeling mechanisms implicated in the precise extension and targeting of axonal arbors still remain mostly unsolved.

Ca^{2+} plays a central role in the regulation of neuronal morphogenesis. It is believed that there is an elevated optimal range for the intracellular Ca^{2+} concentration that supports maximal neurite outgrowth in various types of neurons (Kater et al., 1988; Gomez and Zheng, 2006). Ca^{2+}/calmodulin-dependent protein kinases (CaMKs), a major Ca^{2+}-dependent kinase family, are good candidates as potential downstream effectors of calcium elevation in neurons (Soderling and Stull, 2001; Hudmon and Schulman, 2002). Although the essential role of CaMKII subfamily members in neuronal plasticity has been shown, much less is known about the function of the CaMKI/IV subfamily, which forms several distinct kinase cascades downstream of CaMK kinase α (CaMKKα) and/or CaMKKβ (Soderling, 1999; Hook and Means, 2001; Hudmon and Schulman, 2002; Bito and Takemoto-Kimura, 2003). The CaMKI family includes four isoforms: α (Nairn and Greengard, 1987), β/Pnck (Yokokura et al., 1997), γ/CL3 (Takemoto-Kimura et al., 2003), and δ/CKLiK (Ishikawa et al., 2003). Recently, a few reports from several laboratories, including ours, have started to suggest, *in vitro*, that CaMKI activity may participate in the regulation of neuronal morphology such as growth cone motility (Wayman et al., 2004), neurite outgrowth (Schmitt et al., 2004; Uboha et al., 2007), activity-dependent growth of dendrites (Wayman et al., 2006; Takemoto-Kimura et al., 2007), and stabilization of spines (Saneyoshi et al., 2008). However, evidence based on materials

Received June 25, 2009; revised Aug. 18, 2009; accepted Sept. 29, 2009.

This work was supported in part by grants-in-aid from the Ministry of Education, Culture, Sports, Science and Technology of Japan (S.T.-K., Y.T., T.H., H.O., H.B.) and the Ministry of Health, Labour and Welfare of Japan (H.B.), 21st Century Center of Excellence (COE) and Global COE Programmes (H.B.), by a grant from the National Institutes of Health (T.A.C.), and by awards from the Astellas Foundation for Research on Metabolic Disorders (H.B., S.T.-K.), the Naito Foundation (S.T.-K.), the Cell Science Research Foundation, the Takeda Foundation, and the Toray Science Foundation (H.B.). N.A.-I. and M.N. were predoctoral and postdoctoral fellows funded by Japan Society for the Promotion of Science, respectively. We thank all members of the Bito laboratory for support and discussion, T. Soderling and G. Wayman for constructive comments on a previous version of this work, and M. Kano for initially providing access to a validated working stock of muscimol. We are grateful to H. Tokumitsu (Kagawa University) for CaMKK-β WT and V269F cDNA; to J. Nabekura (National Institute for Physiological Sciences, Aichi, Japan) and K. Nakayama (Showa University, Tokyo, Japan) for a KCC2 plasmid; to R. Y. Tsien (Howard Hughes Medical Institute and University of California, San Diego, La Jolla, CA) for mRFP1 and mCherry cDNAs; and to K. Fukunaga and J. Kasahara (Tohoku University) for a rabbit anti-CaMKIα antibody. BDNF was supplied by Dainippon Sumitomo Pharma Co., Ltd. through the courtesy of C. Nakayama and T. Ishiyama. We are also indebted to assistance from K. Saiki, Y. Kondo, and T. Kinbara.

Correspondence should be addressed to Haruhiko Bito, Department of Neurochemistry, Graduate School of Medicine, University of Tokyo, 7-3-1 Hongo, Bunkyo-ku, Tokyo 113-0033, Japan. E-mail: hbito@m.u-tokyo.ac.jp.

N. Ageta-Ishihara's present address: Division of Biological Sciences, Graduate School of Science, Nagoya University, Furo-cho, Chikusa-ku, Nagoya 464-8602, Japan.

DOI:10.1523/JNEUROSCI.3018-09.2009

 0270-6474/09/2913720-10$15.00/0

from genetically engineered animals is still scarce, and *in vivo* validation of such findings is still much awaited. Furthermore, despite the heavy expression of all CaMKI isoforms in the developing forebrain, there is yet little information as to what kinds of endogenous activity or extracellular ligands may influence the activity of CaMKI, during a perinatal period when only spontaneous Ca^{2+} transients are generated, and when synaptic activity-driven Ca^{2+}-mobilization is still missing.

We previously reported that a dendritic raft-anchored CaMK, CaMKIγ/CL3, plays an essential role in dendritic growth downstream of BDNF (Takemoto-Kimura et al., 2007). However, the exact context in which other CaMKI isoforms might contribute to neuronal morphogenesis remained obscure.

Here, we show genetic and pharmacogenetic evidence that demonstrates that two separate limbs of CaMKK–CaMKI cascades, CaMKK–CaMKIα and CaMKK–CaMKIγ, critically coordinate axonal and dendritic morphogenesis of immature cortical neurons, respectively. Furthermore, we found that activation of $GABA_A$ receptors promoted axonal growth via the CaMKK–CaMKIα pathway. During perinatal brain development, *in vivo* knockdown of CaMKIα significantly impaired the terminal elongation of callosal axon projections in the somatosensory cortex. Together, our data suggest that a GABA-driven CaMK cascade may play a critical role in activity-regulated refinement of cortical axon wiring.

Materials and Methods

Construction of expression plasmids and RNA interference vectors. For RNA interference (RNAi) experiments, short hairpin RNA (shRNA) vectors, coexpressing mRFP1 as a morphological tracer, were constructed essentially as described previously (Takemoto-Kimura et al., 2007). To create pSUPER-shCaMKIα and pSUPER-shCaMKIα#2, two complementary 60 bp oligonucleotides carrying sense and antisense sequences for CATTGTAGCCCTGGATGAC (19 bp; corresponding to nucleotides 231-249 of mouse CaMKIα) and antisense and sense sequences for GATCAAGCACCCCAACATT (19 bp; corresponding to nucleotides 216-234 of mouse CaMKIα), respectively, were subcloned into the pSuper+mRFP1 plasmid backbone. pSUPER-shNega was generated similarly except that an artificial 19-mer sequence (ATCCGCGCGATAGTACGTA) was used as a target as described previously (Takemoto-Kimura et al., 2007). This sequence was based on a commercially available negative control small interfering RNA sequence (B-Bridge International), and we confirmed that it had no significant identity to any known mammalian gene based on a BLAST (basic local alignment search tool) search. Silent mutations were introduced into the shRNA target sequence of enhanced green fluorescent protein (EGFP)-tagged wild-type (WT) and mutant CaMKIα cDNAs to generate shRNA-resistant constructs (pEGFP-$CaMKI\alpha_{res}$ and related constructs). Short hairpin RNA interference vectors against CaMKIα, CaMKIγ/CL3, and CaMKIV [shCaMKIα (this study); shCaMKIγ/CL3 and shCaMKIV (Takemoto-Kimura et al., 2007)] selectively suppressed expression of GFP-CaMKIα, GFP-CaMKIγ/CL3, GFP-CaMKIV, respectively (supplemental Fig. 2*A*,*B*, available at www.jneurosci.org as supplemental material). An antibody against CaMKIV (BD Biosciences Transduction Laboratories) also confirmed these results. The potency of the knockdown was estimated to be ~70–80%, based on the reduction of overexpressed GFP-tagged proteins in Western blot analyses (supplemental Fig. 2*B*, available at www.jneurosci.org as supplemental material). In keeping with this, and consistent with a transfection efficiency of >50% in our electroporation, we also detected a target-specific decrease of 40~50% in the amount of endogenous mRNA using a real-time PCR system (LightCycler 1.5; Roche Diagnostics) (supplemental Fig. 2*C*, available at www.jneurosci.org as supplemental material).

Rat CaMKIα cDNA was inserted into pEGFPC1 vector (Clontech) to generate pEGFP-CaMKIα (Takemoto-Kimura et al., 2003). The expression vector for a constitutively active form, pEGFP-CaMKIαCA (286IHQS to 286EDDD; F307A) was created from pEGFP-CaMKIα by

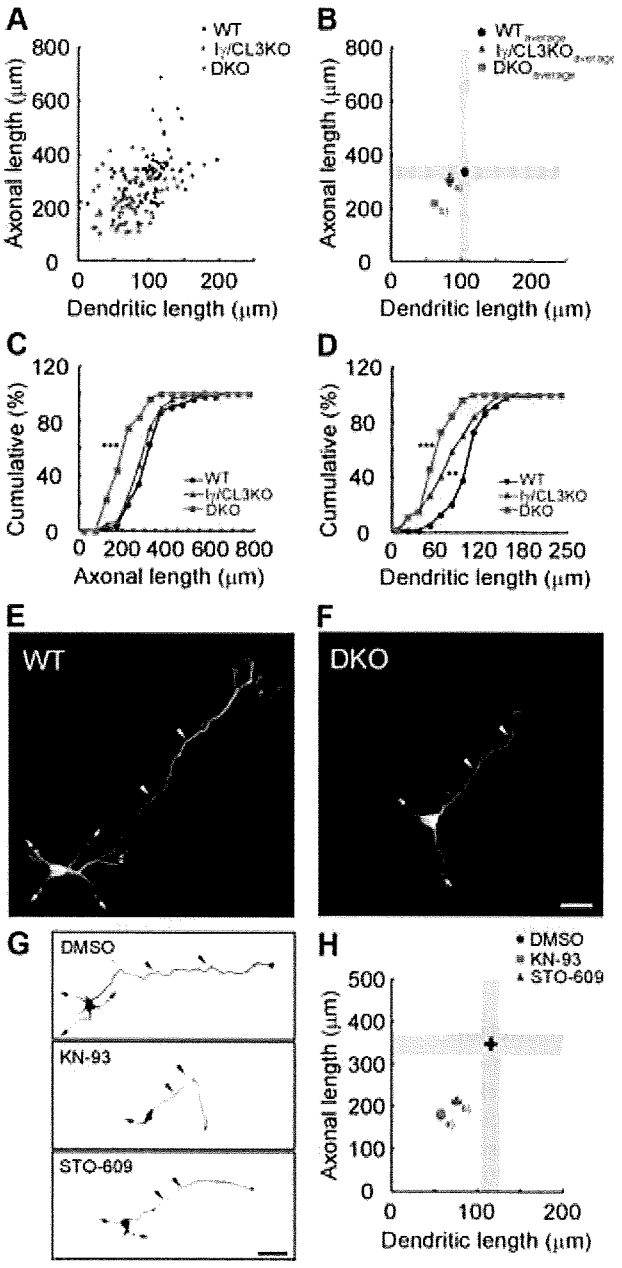

Figure 1. CaMKK-dependent CaMK cascades control cortical axonal and dendritic growth. ***A***, ***B***, A scattered plot (orthogonal plot) of data points (***A***) and averages (***B***) for both axonal and dendritic lengths obtained of individual neurons. Black circles, Wild type (WT). Blue triangles, I-γ/CL3 knock-out (I-γ/CL3 KO). Red squares, CaMKKα/β-double knock-out (DKO). Number of neurons: WT, $n = 52$; I-γ/CL3 KO, $n = 44$; DKO, $n = 52$. [a]Dendrite, $p < 0.01$; [b]Axon, $p < 0.001$; dendrite, $p < 0.001$ (one-way ANOVA with Tukey's test comparison with WT). ***C***, ***D***, Cumulative probability analysis for total axonal length (***C***) and total dendritic length (***D***) in neurons from WT, DKO, and I-γ/CL3 KO mice. Number of neurons: WT, $n = 52$; DKO, $n = 52$; I-γ/CL3 KO, $n = 44$. $^{**}p < 0.01$; $^{***}p < 0.001$, Kolmogorov–Smirnov test comparison with WT. ***E***, ***F***, Cortical neurons (2 d *in vitro*) from CaMKKα/β-DKO mice (***F***) showed impaired growth of axons (arrowheads) and dendrites (arrows) compared with neurons from WT mice (***E***). Scale bar, 25 μm. ***G***, Treatment with KN-93, a general CaMK inhibitor, and STO-609, a blocker of CaMKKα/β, the upstream kinases of all CaMKI/IV, from 6 to 48 h after plating impaired both axonal (arrowheads) and dendritic (arrows) growth. Scale bar, 50 μm. ***H***, An orthogonal plot shows a quantitative analysis of axonal and dendritic morphometric parameters from each neuron. Number of neurons: DMSO, $n = 48$; KN-93, $n = 43$; STO-609, $n = 48$. [a,b]Axon, $p < 0.001$; dendrite, $p < 0.001$ (one-way ANOVA with Tukey's test comparison with DMSO).

site-directed mutagenesis. Similarly, a point mutation was introduced to generate pEGFP-CaMKIαK49A. pCAG-EGFP-CaMKIγ/CL3 was as described previously (Takemoto-Kimura et al., 2007). CaMKKβ wild-type and V269F cDNA (Tokumitsu et al., 2003) (a kind gift from Dr. Hiroshi Tokumitsu, Kagawa University, Kagawa, Japan) was subcloned into pEGFPC3. Mouse CaMKIβ and CaMKIδ cDNAs were obtained from the German RZPD gene collection and RIKEN Genomic Science Center, respectively, and inserted into pEGFPC1 vector to generate pEGFP-CaMKIβ and pEGFP-CaMKIδ. All constructs were verified by sequencing.

Gene targeting, neuronal culture, and pharmacology. All animal experiments in this study were performed in accordance with regulations and guidelines for the care and use of the experimental animals of the University of Tokyo, and approved by the institutional review committee of University of Tokyo Graduate School of Medicine.

CaMKKα-knock-out (KO) mice were described previously (Blaeser et al., 2006). CaMKKβ-KO mice were produced similarly by deleting exon 2 (where the ATG starts) through exon 6 of the CaMKKβ gene. A detailed characterization of CaMKKβ-KO mice will be described elsewhere (F. Blaeser and T. A. Chatila, unpublished observations). CaMKKα- and CaMKKβ-KO mice were crossed to produce CaMKKα/β-double knock-out (DKO) mice. The targeting strategy of CaMKIγ/CL3-KO mice was as described previously (Takemoto-Kimura et al., 2007).

Dissociated cortical neurons were prepared and cultured from embryonic day 19 (E19) Sprague Dawley rats or E17 C57BL/6 mice (wild-type as well as mutant mice), essentially as described previously (Takemoto-Kimura et al., 2007). In brief, dissected cortices were incubated for 10 min with 10 mg/ml trypsin type XI (Sigma-Aldrich) plus 0.5 mg/ml DNase I type IV (Sigma-Aldrich) at room temperature and mechanically dissociated in Hanks solution, pH 7.4 (Sigma-Aldrich), with 0.5 mg/ml DNase I type IV and 12 mM $MgSO_4$. Cortical neurons were transfected immediately after dissociation by electroporation using a Nucleofector (Amaxa Biosystems), plated onto poly-L-lysine-coated 12 mm coverslips (BD Biosciences), poly-D-lysine-coated glass-bottom dishes (MatTek) or six-well dish (BD Biosciences), and maintained in minimum essential medium (Invitrogen) containing 5 g/L glucose, 0.2 g/L $NaHCO_3$, 0.1 g/L transferrin (Calbiochem), 2 mM GlutaMAX-I (Invitrogen), 25 μg/ml insulin (Sigma-Aldrich), B-27 supplement (Invitrogen), and 10% fetal bovine serum. Cultures were maintained in 5% CO_2 at 37°C.

For inhibition and stimulation experiments, 2-[*N*-(2-hydroxyethyl)-*N*-(4-methoxybenzenesulfonyl)] amino-*N*-(4-chlorocinnamyl)-*N*-methylbenzylamine (KN-93) (Calbiochem), 1,8-naphthoylene benzimidazole-3-carboxylic acid (STO-609) (Tocris Bioscience), mevastatin (Wako), muscimol (Tocris Bioscience), or BDNF [generously provided by Dainippon Sumitomo Pharma Co., Ltd. (Osaka, Japan) by courtesy of Dr. Chikao Nakayama] were added to the medium of cultured neurons expressing mRFP1 at 6 h after plating at the final concentrations of 10 μM (KN-93), 2.6 μM (STO-609), 10 μM (mevastatin), 1 μM (muscimol), and 50 ng/ml (BDNF), respectively. Bath application was performed by dissolving the reagents in one-half volume of the conditioned culture medium and by mixing this gently with the remaining one-half of the original medium in the dish. No medium change was done onward until fixation.

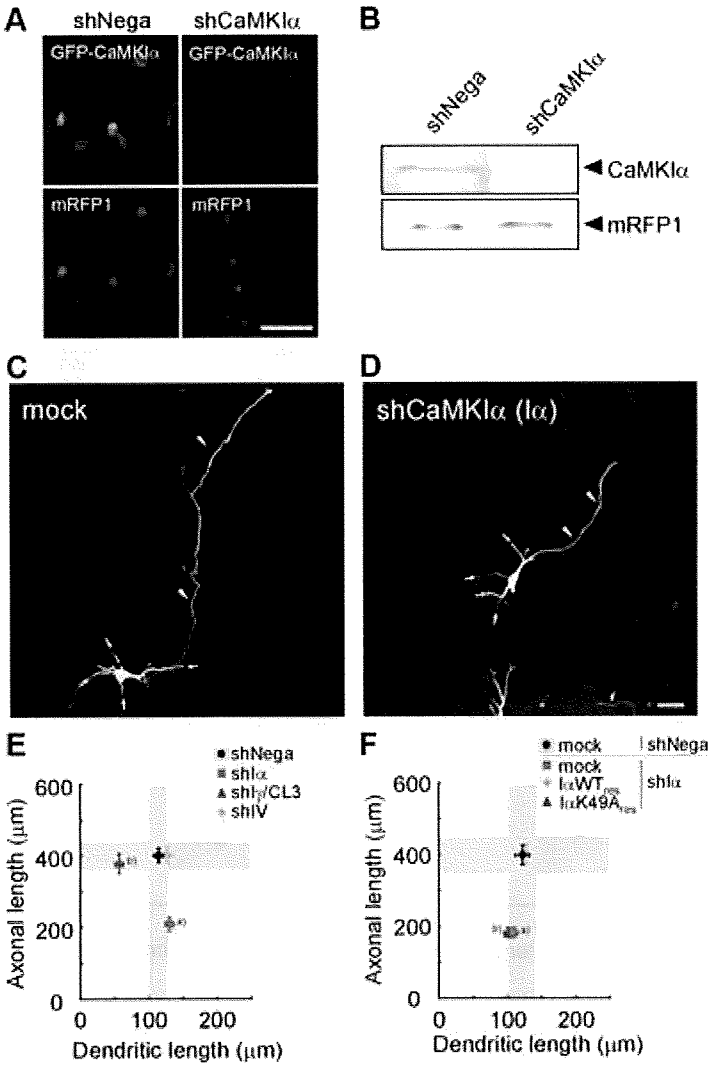

Figure 2. Knockdown of CaMKIα specifically impairs axonal but not dendritic growth. ***A***, Efficient downregulation of exogenous GFP-CaMKIα was achieved by a CaMKIα-targeted shRNA vector (shCaMKIα), but not by a control vector (shNega), in rat cortical neurons. The mRFP1 expression, which was driven by a dual promoter in a pSUPER+mRFP1 vector, remained unchanged. Scale bar, 50 μm. ***B***, Knockdown of endogenous CaMKIα was evaluated by Western blot analysis using an anti-CaMKIα antibody. Rat cortical neurons were transfected with pSUPER-shNega or pSUPER-shCaMKIα by electroporation, and the cells were lysed at 2 DIV. shCaMKIα suppressed endogenous CaMKIα, whereas the control mRFP1 expression level remained unchanged. ***C***, ***D***, shCaMKIα-expressing rat cortical neurons (shCaMKIα) (***D***) showed impaired axonal growth (arrowheads), whereas the dendritic morphology was spared (arrows) compared with neurons from shNega-expressing rat cortical neurons (shNega) (***C***). Scale bar, 25 μm. ***E***, An orthogonal plot of averaged data; $n = 15$ for all groups. [a]Axon, $p < 0.001$. [b]Dendrite, $p < 0.001$ (one-way ANOVA with Tukey's test comparison with shNega). Scale bar, 25 μm. ***F***, Introduction of shCaMKIα-resistant wild-type GFP-CaMKIα (WT_{res}) successfully rescued the axonal defect elicited by shCaMKIα. In contrast, an shCaMKIα-resistant kinase-inactive GFP-CaMKIα (a $K49A_{res}$ point mutant) was unable to rescue the shCaMKIα phenotype. $n = 15$ for all groups. [a,b]Axon, $p < 0.001$ (one-way ANOVA with Tukey's test comparison with shNega + mock).

Immunocytochemistry, morphometric analyses, and visualization of raft-targeted proteins. For morphometric analysis, cortical neurons were transfected immediately after dissociation by electroporation using Nucleofector and plated onto 12 mm poly-L-lysine-coated coverslips at the density of 5×10^5 cells (rats) or 7.5×10^5 cells (mice) per coverslip in 24-well plates. Dissociated cultures of rat and mouse cortical neurons and all measurements (axonal and dendritic length, axonal tip numbers) were performed at 2 d *in vitro* (DIV) essentially as described previously

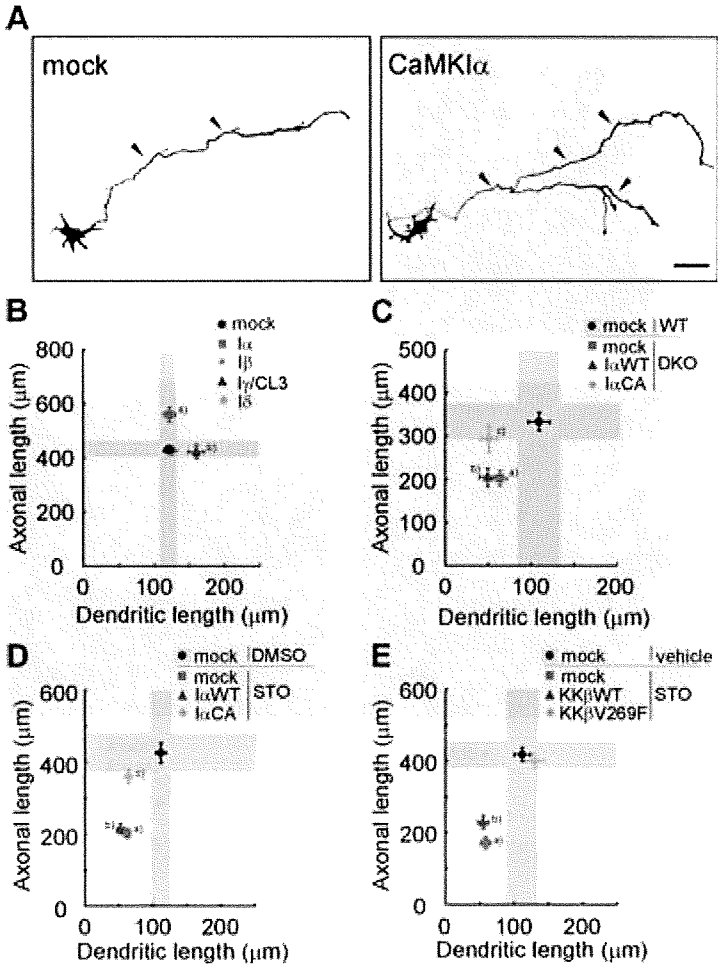

Figure 3. A specific role for a CaMKK–CaMKIα cascade in promoting axonal growth in cortical neurons. ***A***, Representative images of rat cortical neurons transfected with GFP-CaMKIα. Scale bar, 50 μm. ***B***, Overexpression of CaMKIα and CaMKIγ facilitated axonal and dendritic growth, respectively. $n = 15$ for all groups. [a]Axon, $p < 0.001$; [b]dendrite, $p < 0.05$ (one-way ANOVA with Tukey's test comparison with mock). ***C***, The axonal growth defect in DKO mice was selectively rescued by coexpression of a constitutively active CaMKIα (CaMKIαCA), but not by a wild-type CaMKIα (CaMKIαWT); the dendritic growth defect was left unaltered; $n = 15$ for all groups. [a]Axon, $p < 0.01$; dendrite, $p < 0.05$; [b]axon, $p < 0.01$; dendrite, $p < 0.001$; [c]dendrite, $p < 0.01$ (one-way ANOVA with Tukey's test comparison with WT plus mock). ***D***, Only the axonal growth defects caused by STO-609 treatment were rescued by expression of a constitutively active CaMKIα (CaMKIαCA), but not of a wild-type CaMKIα (CaMKIαWT). Dendritic growth defects remained unchanged; $n = 15$ for all groups. [a,b]Axon, $p < 0.001$; dendrite, $p < 0.001$; [c]Dendrite, $p < 0.001$ (one-way ANOVA with Tukey's test comparison with DMSO plus mock). ***E***, Both axonal and dendritic growth defects caused by STO-609 treatment were rescued by introducing an STO-609-resistant CaMKKβ mutant (V269F), but not a CaMKKβ-WT. n = 15 for all groups. [a,b]Axon, $p < 0.001$; dendrite, $p < 0.01$ (one-way ANOVA with Tukey's test comparison with vehicle plus mock).

(Takemoto-Kimura et al., 2007). Images of neuronal morphologies were captured based on immunoreactivities against GFP, mRFP1, or mCherry, using the Olympus BX51 microscopy system with a 20× objective. Dendrites and axons were identified by standard morphological criteria as described previously (Takemoto-Kimura et al., 2007), and only neurons that possessed one clearly classifiable axon and one or more dendrites were analyzed. All quantitative analyses were performed by an observer blinded to the identity of the transfected constructs, genotypes of mice, or treated drugs.

Immunostaining was performed as described previously (Bito et al., 1996; Nonaka et al., 2006; Takemoto-Kimura et al., 2007). A rabbit anti-DsRed antibody (Takara) was used for quantitative morphometric analyses of RNAi, rescue, and forced expression experiments, and a rat anti-GFP antibody (Nacalai Tesque) was used to detect coexpressed constructs. An anti-GM130 antibody (BD Biosciences Transduction Laboratories) was used as a Golgi marker. As secondary antibodies, Alexa 488-, Alexa 594-conjugated anti-mouse, anti-rabbit, and anti-rat IgG antibodies (Invitrogen) were used. Fluorescent images were taken by a confocal laser microscopy system (LSM 510META-V3.2; Carl Zeiss) built on an inverted microscope (Axiovert 200M; Carl Zeiss) with the 40× objective [Plan-Neofluar 40×/numerical aperture (NA) 1.3, oil; Carl Zeiss] or using a CCD camera-based imaging analysis system (an Olympus BX51 equipped with a DP-70 camera). Visualization of raft-targeted proteins was performed as described previously (Takemoto-Kimura et al., 2007).

Western blot analysis. For Western blot analysis, cortical neurons were transfected with pSUPER-shNega or pSUPER-shCaMKIα by electroporation using a Nucleofector and plated at a density of 5×10^6 cells in a six-well dish. At 2 DIV, the cells were lysed in lysis buffer containing 50 mM Tris-HCl, pH 6.8, 2% SDS, and 10% glycerol. A rabbit anti-CaMKIα antibody (Uezu et al., 2002) was used (a kind gift from Drs. Kohji Fukunaga and Jiro Kasahara, Tohoku University, Sendai, Japan). Chemiluminescence detection was performed using horseradish peroxidase-conjugated anti-rabbit IgG and ECL Plus reagent (GE Healthcare).

Calcium imaging. Fluorescent calcium imaging was performed essentially as described previously (Furuyashiki et al., 2002; Takemoto-Kimura et al., 2007). Twenty-four hours after plating, cortical neurons on glass-bottom dishes were loaded with Fluo-4 AM (2.5 μM; Dojindo Laboratories) for 30 min at room temperature. After wash, cells were incubated at 37°C in a stage CO_2 chamber (Tokai Hit Co., Ltd.) equipped on an LSM 510 META (Carl Zeiss). After baseline recording, a medium containing 20× muscimol (final concentration, 1 μM) was gently bath-applied. Fluorescence changes in the cell bodies of individual cells were analyzed using MetaMorph or ImageJ software, and data are expressed as $\Delta F/F_0$.

In utero *electroporation, data acquisition, and quantification of the terminal arborization of callosal axons. In utero* electroporation was performed as described previously (Mizuno et al., 2007). Equal amount of pSUPER-vectors (2 μg/μl) and pCAG-EGFP (2 μg/μl) were mixed together with the dye Fast Green (0.05%; Wako) for injection into the lateral ventricle. The postnatal brains [postnatal day 16 (P16)] were fixed by transcardial perfusion of 4% PFA in 0.1 M phosphate buffer followed by overnight immersive fixation in 4% PFA in PBS and then transferred to 30% sucrose in PBS for 1–2 d at 4°C. Serial coronal brain sections were prepared at 50 μm thickness by a cryostat (HM560; Microm), and every one section out of four was immunostained. Sections were permeabilized in 0.3% Triton X-100 in PBS, and then blocked in 5% normal goat serum, 1% BSA, and 0.3% Triton X-100 in PBS followed by fluorescent immunostaining of EGFP. Sections were counterstained with DAPI (4′,6′-diamidino-2-phenylindole) (Invitrogen). Quantitative analyses were performed and compared using the utmost posterior section of the stained sets that included the corpus callosum.

Confocal images were taken (LSM 510META-V3.2; Carl Zeiss) with a 10× objective (Plan-Neofluar 10×/NA 0.3; air; Carl Zeiss) with 10 μm optical sectioning. *Z* projection images taken at 512 × 512 pixels were acquired by average projection mode and background was subtracted, and the intensity was normalized by maximal intensity in the white mat-

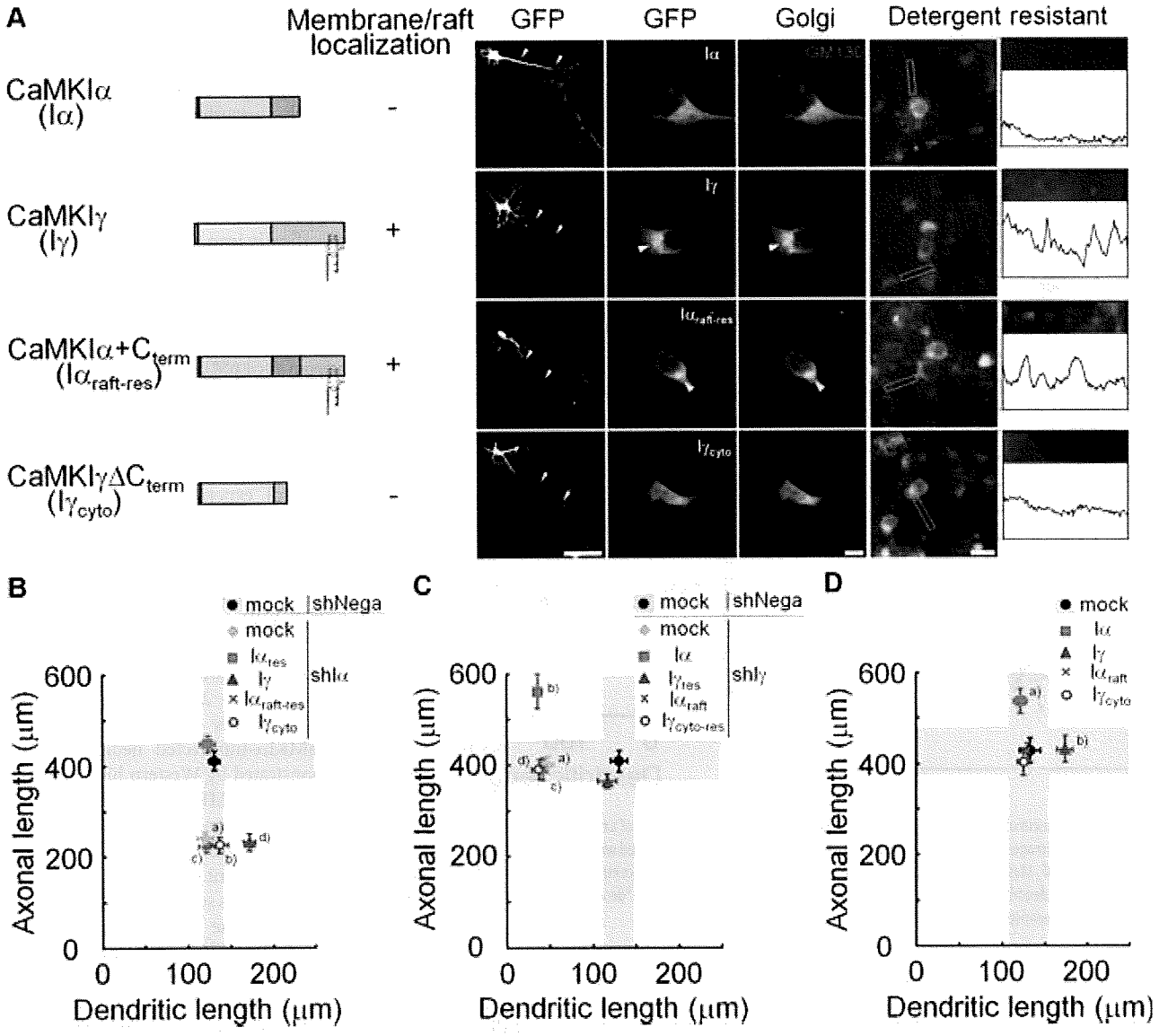

Figure 4. Functional segregation of CaMKK–CaMKIα and CaMKK–CaMKIγ cascades. ***A***, The domain structures and subcellular localizations of CaMKIα (Iα), CaMKIγ/CL3 (Iγ), and their chimeras. GFP-CaMKIα (Iα), CaMKIγ/CL3 (Iγ), and their chimeras distribution detected by anti-GFP immunostaining showed colocalization with a Golgi marker, GM130. GFP-Iγ and $I\alpha_{raft\text{-}res}$ signals were also enriched within Golgi (arrowheads). Single representative confocal sections are shown for Golgi localization. GFP-Iγ and -$I\alpha_{raft\text{-}res}$ fluorescence was retained after detergent treatment in a punctate manner in 2 DIV cortical neurons along the dendrites, demonstrating a sizable portion of detergent-resistant GFP-Iγ and $I\alpha_{raft\text{-}res}$ in the dendritic rafts. Line scans of pixel fluorescence, performed within a chosen field of a 15 μm dendritic segment. Scale bars: right, 50 μm; middle, 5 μm; left, 100 μm. ***B***, Neither Iγ, $I\alpha_{raft\text{-}res}$, nor $I\gamma_{cyto}$ were able to rescue the axonal phenotype caused by knockdown of CaMKIα; $n = 15$ for all groups. ^{a,b,c}Axon, $p < 0.001$; ^{d}axon, $p < 0.001$, dendrite, $p < 0.01$ (one-way ANOVA with Tukey's test comparison with shNega plus mock). ***C***, Neither Iα, $I\alpha_{raft}$, nor $I\gamma_{cyto\text{-}res}$ were able to rescue the dendritic phenotype caused by knockdown of CaMKIγ/CL3; $n = 15$ for all groups. ^{a,c,d}Dendrite, $p < 0.001$; ^{b}axon, $p < 0.001$, dendrite, $p < 0.001$ (one-way ANOVA with Tukey's test comparison with shNega plus mock). ***D***, Overexpression of CaMKIα, specifically increased axon length in cortical neurons; $n = 15$ for all groups; $n = 15$ for all groups. ^{a}Axon, $p < 0.05$; ^{b}dendrite, $p < 0.001$ (one-way ANOVA with Tukey's test comparison with mock).

ter. For one-dimensional fluorescence intensity profile analysis in Figure 7*C*, a rectangular zone (nominal width set at 100 pixels) was drawn along the vertical axis from the pial surface to the white matter, and the average pixel intensity projected onto the vertical axis was calculated. To quantify the impairment of the cortical wiring in Figure 7*D*, average intensity in a rectangle region (100 pixels in width) in the cortex was divided by that in the white matter. Three to five pups were used for quantification. All calculations were performed using MetaMorph software (version 7; Molecular Devices).

Statistical analyses. Statistical analyses were run separately for axonal and dendritic datasets throughout our study, while using scattered diagrams of paired data of axonal and dendritic lengths ("orthogonal plots"). Statistical analyses were performed using Prism 4.0 (GraphPad Software). Student's *t* test was used for comparisons of two groups. One- or two-way ANOVA with *post hoc* Tukey–Kramer or Bonferroni's test was used for factorial analysis among more than three groups. Kolmogorov–Smirnov test was applied to Figure 1, *C* and *D*. All data are shown as mean ± SEM, unless otherwise mentioned, and shaded regions in orthogonal plots graphically depict the zone of mean ± 2SEM on both axes to facilitate the evaluation of the phenotypes.

Results

CaMKK pathway regulates axonal and dendritic growth during early stages of cortical development

We previously reported that a dendritic raft-anchored CaMKIγ/CL3 (Takemoto-Kimura et al., 2003) plays an essential role in

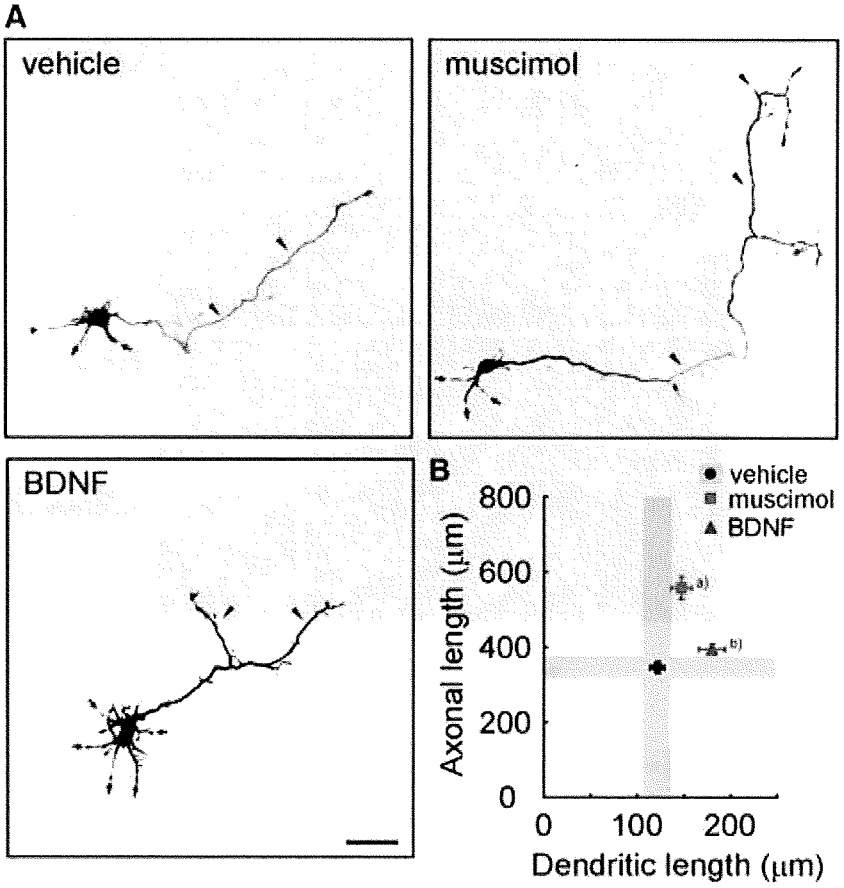

Figure 5. Muscimol, a $GABA_A$ receptor agonist, specifically stimulates elongation of axons in cultured cortical neurons. ***A***, ***B***, Representative images (***A***) and ensemble data (***B***) of immature cortical neurons treated with either muscimol (a $GABA_A$ receptor agonist) or BDNF. Muscimol significantly promoted axonal growth (arrowheads). In contrast, BDNF had no effect on axons but mainly affected dendrites. Scale bar, 50 μm. $n = 15$ for all groups. [a]Axon, $p < 0.001$; [b]dendrite, $p < 0.01$ (one-way ANOVA with Tukey's test comparison with vehicle).

dendritic growth downstream of BDNF during the morphological maturation of cortical neurons (Takemoto-Kimura et al., 2007). As four distinct CaMKI isoforms (α, β, γ/CL3, and δ) and CaMKIV are activated by upstream CaMKKs α and β, we sought to test how potently neuritogenesis was disturbed in cultured cortical neurons generated from CaMKKα/β-DKO mice. To specifically identify the genotype contribution to either axonal or dendritic growth, we orthogonally plotted the dendritic length (i.e., total length of all dendritic processes) and axonal length (i.e., total length of all axonal processes including branches) for each GFP-expressing cortical neuron blindly chosen from multiple fields of view (Fig. 1*A*,*B*; supplemental Fig. 1, available at www.jneurosci.org as supplemental material). Although cortical neurons from CaMKIγ/CL3 knock-out mice revealed a strikingly dendrite-specific deficit (Fig. 1*A–D*), we found that both axons and dendrites were significantly shortened in cortical neurons from DKO mice, compared with neurons from WT mice (Fig. 1*A–F*). Exposure to KN-93, which blocks all CaMK species (CaMKII, CaMKI, CaMKIV, and CaMKK), also reduced both total axonal and dendritic lengths (Fig. 1*G*,*H*). Specific blockade of the CaMKKs, using STO-609, a selective inhibitor for CaMKKs (Tokumitsu et al., 2002), resulted in a quantitatively similar impairment (Fig. 1*G*,*H*). Together, these genetic and pharmacological experiments clearly demonstrated that CaMKK-mediated CaMK cascades played critical roles both in axonogenesis and dendritogenesis of immature cortical neurons, consistent with a previous work on other cell types (Wayman et al., 2004). Furthermore, our data pointed to the presence of a selective CaMKK–CaMK cascade that strongly supported cortical axonal growth in a manner that was distinct from the dendritic contribution of CaMKIγ.

Suppression of CaMKIα expression specifically impairs axonal but not dendritic growth

To identify which of CaMKI or CaMKIV isoform(s) was involved in regulation of the axonal growth, we designed several short hairpin-type pSUPER vectors that were targeted to specific isoforms of the CaMKI/IV subfamily members. In this RNAi experiment, we also coexpressed a PGK promoter-driven mRFP1 as a morphological tracer. In a control experiment, polarized cortical neurons grown for 48 h typically grew 5~6 dendrites and a single axon. Knockdown using an shCaMKIα vector was prominent enough such that even an overexpressed GFP-CaMKIα became barely detectable 48 h after transfection, whereas the control mRFP1 expression level remained unchanged (Fig. 2*A*). Strong suppression of endogenous CaMKIα expression in shCaMKIα-transfected neurons was also demonstrated by Western blot analysis using an anti-CaMKIα antibody (Fig. 2*B*). A lack of cross-knockdown effects across α-, γ-CaMKI isoforms and CaMKIV was verified (supplemental Fig. 2, available at www.jneurosci.org as supplemental material).

Under these conditions, shCaMKIα-treated neurons showed unchanged dendritic growth but had a markedly shorter axon (Fig. 2*C*,*D*). Under the same conditions, in contrast, CaMKIγ/CL3 knockdown specifically blocked dendritic, but not axonal, outgrowth (Fig. 2*E*) (Takemoto-Kimura et al., 2007), whereas CaMKIV knockdown had no effect (Fig. 2*E*). The striking specificity in the axonal phenotype of CaMKIα was replicated even when axonal growth was measured under conditions in which shCaMKIα-transfected neurons were kept in suspension culture for an extended period (48 h) before plating, to ensure a maximized knockdown efficiency (supplemental Fig. 3, available at www.jneurosci.org as supplemental material). The impairment in axonal growth observed in CaMKIα-diminished neurons was rescued by expression of an shCaMKIα-resistant WT-CaMKIα (WT_{res}), but not by that of an shCaMKIα-resistant kinase-inactive CaMKIα ($K49A_{res}$), demonstrating the requirement of the kinase activity of CaMKIα (Fig. 2*F*). Together, our results strongly implicated the CaMKK–CaMKIα cascade as a critical player in the control of cortical axonal growth.

Two separate CaMKK–CaMKI cascades control cortical axonal and dendritic growth

In keeping with this robust selectivity in the knockdown experiments, forced expression of either one of the four CaMKI isoforms revealed that total axonal length was stimulated only by an

increase in CaMKIα, whereas dendrite growth was promoted only by CaMKIγ/CL3 expression (Fig. 3*A*,*B*). No change in primary axon number was detected in CaMKIα-overexpressing neurons, suggesting that CaMKIα did not act on axon specification per se (data not shown). Most critically, expression of a constitutively active CaMKIα (CaMKIαCA), was sufficient to rescue the axonal deficit, but without altering dendritic atrophy, in cortical neurons from DKO mice (Fig. 3*C*) or in WT neurons treated with STO-609 (Fig. 3*D*). However, forced expression of CaMKIαWT, which enzymatically remains inactive in the absence of CaMKK activity, had no effect in either of these backgrounds (Fig. 3*C*,*D*). In a parallel experiment, both axonal and dendritic defects in WT neurons treated with STO-609 were rescued by transfection of a STO-609-resistant CaMKKβ V269F mutant (Tokumitsu et al., 2003) (Fig. 3*E*).

Together, these data strongly implicated the CaMKK–CaMKIα and CaMKK–CaMKIγ cascades as parallel pathways acting independently in the promotion of axonal and dendrite growth, respectively, in cultured cortical neurons.

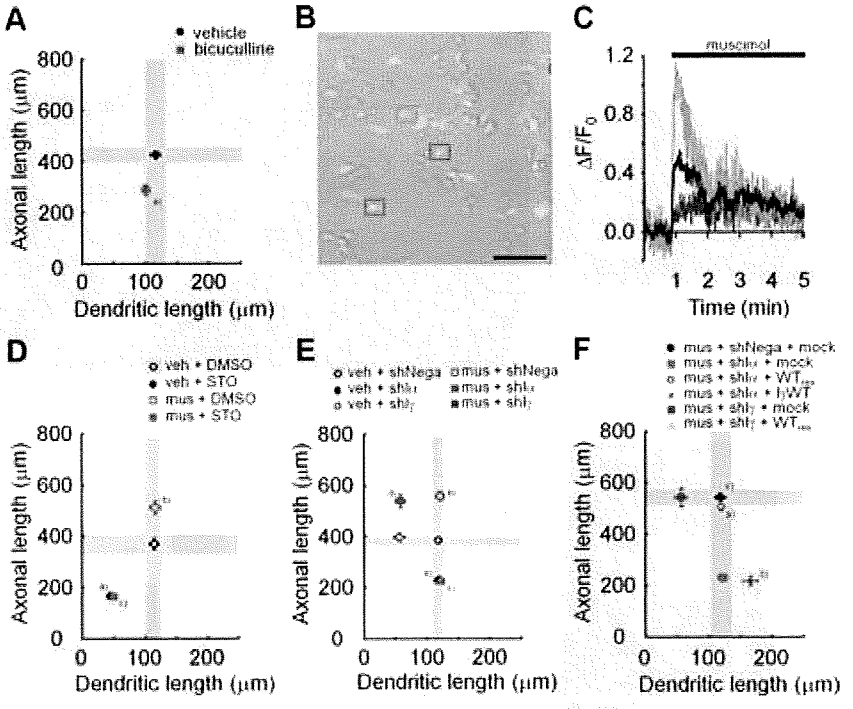

Figure 6. Activation of $GABA_A$ receptors promotes axonal growth via the CaMKK–CaMKIα pathway in immature cortical neurons. ***A***, Bicuculline, a $GABA_A$ receptor antagonist, blocked axonal growth; $n = 15$ for all groups. [a]Axon, $p < 0.001$ (Student's *t* test comparison with vehicle). ***B***, Embryonic cortical neurons (1 DIV) were loaded with a calcium indicator, Fluo-4 AM, and calcium responses were measured by time-lapse imaging. A green fluorescence image was overlaid on a differential interference contrast image. The colored boxes indicate the location of cells shown in ***C***. Scale bar, 50 μm. ***C***, Representative calcium responses in individual cells after muscimol administration. Three different types of calcium responses were revealed (green, blue, and red). An averaged response from 10 cells in a microscopic field is revealed in black. ***D***, Both basal and muscimol-stimulated axonal growths were suppressed with STO-609, a specific blocker of CaMKKα/β; $n = 15$ for all groups. Axon: two-way ANOVA, muscimol effect, $F_{(1,56)} = 14.38, p = 0.0004$; drug effect, $F_{(1,56)} = 225.63, p < 0.0001$; muscimol × drug, $F_{(1,56)} = 15.79, p = 0.0002$. Dendrite: two-way ANOVA, muscimol effect, $F_{(1,56)} = 0.39$, $p = 0.5336$; drug effect, $F_{(1,56)} = 105.76$, $p < 0.0001$; muscimol × drug, $F_{(1,56)} = 0.13, p = 0.7199$. [a,b]Axon, $p < 0.001$ (comparison with vehicle plus DMSO); [c]axon, $p < 0.001$ (comparison with muscimol plus DMSO); n.s. (comparison with vehicle plus STO). ***E***, CaMKIα knockdown quantitatively inhibited axonal growth induced by muscimol treatment, to an extent similar to that obtained with STO-609; $n = 15$ for all groups. Axon: two-way ANOVA, muscimol effect, $F_{(1,84)} = 66.44, p < 0.0001$; RNAi effect, $F_{(2,84)} = 168.04, p < 0.0001$; muscimol × RNAi, $F_{(2,84)} = 19.96, p < 0.0001$. Dendrite: two-way ANOVA, muscimol effect, $F_{(1,84)} = 0.23, p = 0.6305$; RNAi effect, $F_{(2,84)} = 61.58$, $p < 0.0001$; muscimol × RNAi, $F_{(2,84)} = 0.01, p = 0.9888$. [a,b]Axon, $p < 0.001$ (comparison with vehicle plus shNega); [c]axon, $p < 0.001$ (comparison with muscimol plus shNega); n.s. (comparison with vehicle plus shIα); [d]axon, $p < 0.001$ (comparison with vehicle plus shIγ); n.s. (comparison with muscimol plus shNega). ***F***, Introduction of shCaMKIα-resistant wild-type GFP-CaMKIα (WT_{res}) specifically rescued the suppression of muscimol-induced axonal growth triggered by knockdown of CaMKIα; $n = 15$ for all groups. [a]Axon, $p < 0.001$; dendrite, n.s.; [b]axon, n.s.; dendrite, $p < 0.001$ (one-way ANOVA with Tukey's test comparison with muscimol plus shIα plus mock); [c]axon, n.s.; dendrite, $p < 0.001$ (*t* test comparison with muscimol plus shIγ plus mock).

Both localization and kinase specificity of CaMKIα play important roles in CaMKIα-dependent axonal growth

Our data, so far, suggested that the axonogenic action of CaMKIα manifested in a manner that was completely orthogonal and independent to the dendritogenic effect mediated by CaMKIγ/CL3, despite a high degree of structural identity (71% amino acid identity in the catalytic domain sequences). What then discriminated the distinct function of these two kinases?

To identify the molecular determinants involved in axonogenic and dendritogenic selectivity of the CaMKK–CaMKI cascades, we generated CaMKIα/γ chimeras such that each kinase domain was paired with either cytosolic or Golgi/raft localization signals in the C terminus (Fig. 4*A*) (Takemoto-Kimura et al., 2007). We then tested their potencies to rescue the defect caused by knockdown of endogenous CaMKIα. As expected, forced expression of an shCaMKIα-resistant WT-CaMKIα ($Iα_{res}$) rescued the axonal impairment in CaMKIα knockdown neurons (Fig. 4*B*). The WT-CaMKIγ/CL3 (Iγ), however, promoted dendritic growth without showing any effect on axonal deficit. CaMKIα is believed to be freely diffusible. However, the C-terminal region of CaMKIγ/CL3 is lipidified by prenylation and palmitoylation, targeting it preferentially into lipid rafts, which are highly abundant in dendrites and in Golgi (Takemoto-Kimura et al., 2007) (Fig. 4*A*; supplemental Fig. 4, available at www.jneurosci.org as supplemental material). A dendritic raft-targeted mutant of CaMKIα, GFP-CaMKIα+C_{term} ($Iα_{raft\text{-}res}$), was unable to rescue the axonal impairment in CaMKIα knockdown neurons (Fig. 4*B*). A cytoplasmic, raft-excluded mutant of CaMKIγ/CL3, namely CaMKIγ/ CL3ΔC_{term} ($Iγ_{cyto}$), had no ability, either (Fig. 4*B*), contrary to our expectations. Thus, surprisingly, CaMKI-mediated selectivity of neurite growth might not be simply determined by the localization of a CaMKIα or CaMKIγ in or out of the membrane rafts.

To further confirm this, the chimeras were expressed in the background of CaMKIγ/CL3-knockdown neurons. Expression of an RNAi-resistant WT-CaMKIγ/CL3 ($Iγ_{res}$) rescued the dendritic impairment, whereas WT-CaMKIα (Iα) promoted axonal growth without an effect on dendrite impairment (Fig. 4*C*). Again, however, neither a freely diffusible CaMKIγ/CL3ΔC_{term} ($Iγ_{cyto\text{-}res}$), nor a raft-targeted CaMKIα, CaMKIα+C_{term} ($Iα_{raft}$), had any effect (Fig. 4*C*). Furthermore, forced expression of CaMKIα, CaMKIγ, and CaMKIα/γ chimeras in a naive background revealed that total axonal length was stimulated only by

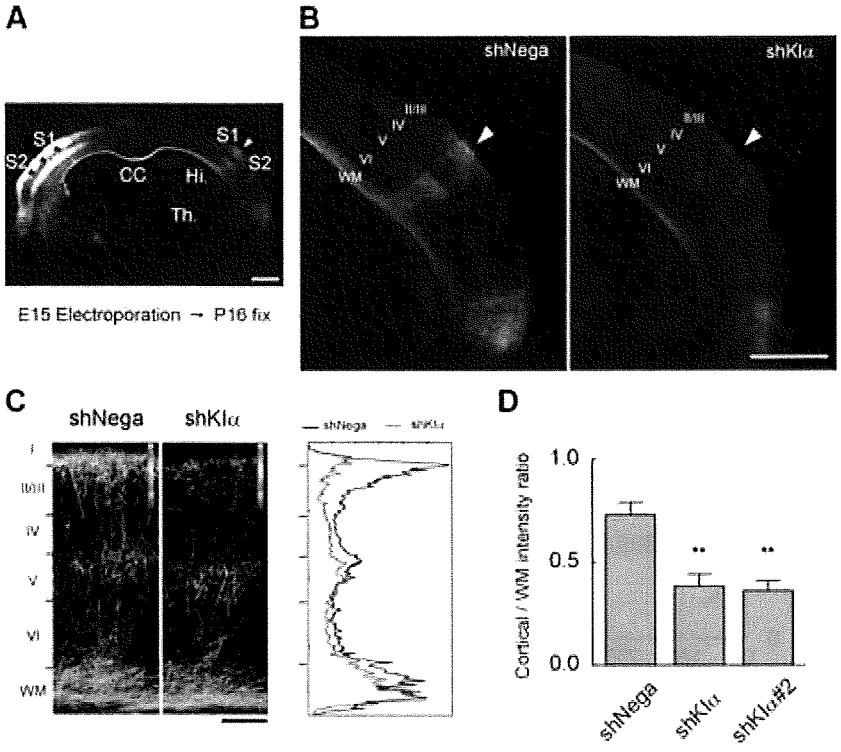

Figure 7. Knockdown of CaMKIα impairs terminal extension of callosal axons *in vivo*. ***A***, A control coronal section was obtained near the posterior end of the corpus callosum, from a P16 pup electroporated *in utero* with pSUPER-shNega and pCAG-EGFP on E15.5. The somatodendritic regions of layer II/III neurons were strongly labeled (asterisks) in the somatosensory cortex, from which callosal axons projected toward the contralateral cortical areas at the S1/S2 border region (arrowhead). Scale bar, 1 mm. CC, Corpus callosum; Hi, hippocampus; Th, thalamus. ***B***, Terminal extension of callosal axons into the contralateral cortical layers was severely disrupted in CaMKIα-knockdown neurons (shKIα), although axons were able to reach the white matter (WM) beneath S1/S2 area (arrowhead). Scale bar, 1 mm. ***C***, Axonal extension and terminal branch arborization were strongly impaired in layers II/III in CaMKIα-knockdown neurons, as illustrated by the magnified images of GFP marker showing the total axonal volumes present in the cortical layers (in pseudocolor), or by a one-dimensional fluorescence intensity profile analysis. Scale bar, 200 μm. ***D***, Quantification of the cortical wiring defect caused by an aberrant terminal axon extension in the cortex. Two independent RNAi constructs (shKIα and shKIα #2) gave similar results. $^{**}p < 0.01$ (one-way ANOVA with Tukey's test comparison with shNega).

an increase in CaMKIα (Fig. 4*D*). Together, these data provide strong functional evidence in support of the notion that CaMKK–CaMKIα and CaMKK–CaMKIγ are not duplicative mechanisms with simply altered targeting of downstream kinases, but are genuinely segregated cascades that are divergent at the level of kinase substrate specificity.

GABA is one of the physiological ligand acting upstream of CaMKIα to promote axonal growth during early stages of cortical development

The biological significance of this specificity could be demonstrated if the physiological signal triggering the axonogenic effect of CaMKIα was identified. To this end, we searched for a potential extracellular ligand that induced intracellular calcium elevation and potently stimulated axonal growth. We found that muscimol, a $GABA_A$ receptor agonist with a known excitatory action during perinatal development (Owens et al., 1996; Represa and Ben-Ari, 2005), specifically promoted elongation of axons, but not of dendrites, in cultured cortical neurons (Fig. 5*A*,*B*). Under the same conditions, we confirmed that BDNF had a complementary growth effect mostly selective for dendrites (Takemoto- Kimura et al., 2007).

To test the extent of requirement for GABA, we added bicuculline, a $GABA_A$ receptor antagonist, in the medium and found that axonal growth was rather selectively impaired (Fig. 6*A*). Furthermore, we confirmed that muscimol application triggered a strong Ca^{2+} influx in our cortical neurons (Fig. 6*B*,*C*). In keeping with this, forced expression of KCC2, a neuronal K^+/Cl^- cotransporter that lowers intracellular Cl^- concentration, and that is upregulated during development to convert the GABA action from excitation to inhibition (Rivera et al., 1999), impaired both constitutive and muscimol-stimulated axonal growth (supplemental Fig. 5, available at www.jneurosci.org as supplemental material). Pharmacological blockade of all CaM kinases using KN-93 (supplemental Fig. 6, available at www.jneurosci.org as supplemental material), or of CaMKK using STO-609 (Fig. 6*D*), completely blocked the axonogenic muscimol effect. CaMKIα RNAi (shIα), but not CaMKIγ/CL3 RNAi (shIγ), selectively impaired muscimol-stimulated axonal growth (Fig. 6*E*), and this effect was rescued by coexpressing an shCaMKIα-resistant CaMKIα WT ($I\alpha WT_{res}$), but not CaMKIγ/CL3 WT (IγWT) (Fig. 6*F*). Thus, a CaMKK–CaMKIα cascade may critically mediate $GABA_A$-stimulated axon outgrowth during the early development of a cortical neuron.

Contribution of CaMKIα in fine-tuning axonal pathfinding *in vivo*

We finally tested the *in vivo* relevance of these findings by investigating the function of CaMKIα during activity-dependent cortical wiring *in vivo*. The callosal axons that originate from layer II/III pyramidal neurons of the somatosensory cortex are known to elongate and target themselves to the border between the S1 and S2 areas of the contralateral cortex, where they suddenly turn and grow into the cortical layers and develop their terminal branches mainly at layers II–III and V. Previous reports demonstrated that reduction of neuronal excitability by overexpression of an inwardly rectifying potassium channel, Kir2.1, impaired such layer-specific development of the terminal branches in the visual cortex (Mizuno et al., 2007) and in the somatosensory cortex (Wang et al., 2007). Furthermore, premature elimination of excitatory GABA drive by forced expression of KCC2 or knockdown of NKCC1 in newly born cortical neurons dramatically perturbed the morphological maturation of the dendrites (Cancedda et al., 2007; Wang and Kriegstein, 2008) or of the terminal callosal axon branches (H. Mizuno, T. Hirano, and Y. Tagawa, unpublished data).

If the morphogenetic effect of excitatory GABA required Ca^{2+} signaling, could the CaMKK–CaMKIα pathway perhaps mediate activity-dependent control of callosal axonal extension? To test this, CaMKIα was knocked down in the somatosensory layer II/III neurons by *in utero* electroporation at E15.5, and an effect on axonal growth was examined. At P16, control neurons terminated their axons into a restricted region (border of S1/S2 area) in the contralateral cortex and extensively developed their terminal

branches into layers II/III and V (Fig. 7*A*). CaMKIα-knockdown neurons extended interhemispheric axonal projections in the white matter, suggesting the CaMKIα may not be absolutely required for midline crossing and progression of axon fibers (Fig. 7*B*). However, their terminal axonal extension into the cortical layers was severely diminished, especially in layers II/III (Fig. 7*C*,*D*). These results indicate a developmentally critical role of CaMKIα in activity-dependent regulation of cortical connectivity *in vivo*.

Discussion

Differential control of cortical axonogenesis and dendritogenesis by activation of CaMKIα and CaMKIγ/CL3

In a previous work (Takemoto-Kimura et al., 2007), we showed that a lipid-modified CaM kinase CaMKIγ/CL3 (a membrane-anchored CaMKI isoform) was directed to the dendrites on raft insertion and could potently promote early dendritic development, with little effect on axon outgrowth, in cultured cortical neurons. In striking contrast to CaMKIγ/CL3, we here demonstrate that a cytosolic sister kinase, CaMKIα, has a complementary role: it has little role in dendritogenesis, but is necessary and sufficient to promote axonogenesis in the same preparation. Additionally, our present work established that CaMKIα regulates axonal extension *in vivo*. Additional rigorous quantitative studies are awaited to establish the potential role of other CaMKK–CaMK signaling pathways in cortical neuritogenesis in general.

How can such specificity of axonal/dendritic growth be regulated by two separate yet structurally resembling kinases lying downstream of the same CaMKKs? The chimeric kinase experiments (Fig. 4) strongly suggested that the diverging kinase substrate specificities and the dissimilarity in subcellular localization (cytosol vs dendritic rafts) might provide a basis for the strikingly differential effect of CaMKIα and CaMKIγ/CL3 during axonal and dendritic development. In support of this functional segregation between the two distinct CaMKK–CaMKI cascades, we identified an extracellular ligand, GABA, which specifically stimulated axonal growth via CaMKIα (this study), whereas BDNF selectively promoted dendritic growth via CaMKIγ (Takemoto-Kimura et al., 2007), during an early developmental stage of cortical neurons.

In principle, BDNF could rather selectively act on dendrites in part because of the strong affinity of the active TrkB receptor to lipid rafts (Suzuki et al., 2004), which are enriched on dendrites. At this point, however, how GABA stimuli could possibly generate an axon-specific effect remains rather unclear, although preliminary Ca^{2+} imaging experiments indicated that $GABA_A$ stimulation might trigger growth cone-localized Ca^{2+} transients (S. Kamijo, H. Fujii, S. Takemoto-Kimura, and H. Bito, unpublished data). It is noteworthy that many potential *in vitro* substrates of CaMKIα have previously been associated with axonal or presynaptic functions. These include synapsin I (Nairn and Greengard, 1987), Numb and Numbl (Tokumitsu et al., 2005), microtubule affinity regulating kinase 2 (MARK2/Par-1b) (Uboha et al., 2007), and β-Pak-interacting exchange factor (βPIX) (Saneyoshi et al., 2008). Although some of these known substrates of CaMKI may potentially underlie a part of early axonal growth, additional work is clearly needed to fully elucidate how an axonogenic substrate may be activated via phosphorylation by CaMKIα.

A pivotal role for a GABA-driven CaMKK–CaMKIα cascade in controlling axonal morphogenesis during early development

In this work, we identified a crucial role for GABA in controlling cortical axon outgrowth during early development via a CaMKK–CaMKIα cascade. In immature cortical neurons, what is the mechanism by which GABA can stimulate axonal development in a CaMKI-dependent manner? Recent studies showed that $GABA_A$ receptors activation has potent excitatory effects in immature, but not in mature, neurons (Ben-Ari et al., 2007). The excitatory action of GABA was demonstrated to be caused by a high basal Cl^- concentration in immature neurons, because of a high amount of the Na^+–K^+–$2Cl^-$ cotransporter (NKCC1) which favors Cl^- influx, whereas the K^+–Cl^- cotransporter (KCC2) primarily responsible for Cl^- efflux is still low in expression (Payne et al., 2003). Because of elevated intracellular Cl^- concentration in immature neurons, $GABA_A$ receptors activation thus induces depolarization (Ben-Ari et al., 2007), thereby likely triggering the opening of voltage-gated Ca^{2+} channels, which then generates enough Ca^{2+} influx leading to CaMKK–CaMKIα activation.

During early development, it is now known that GABA controls a variety of biological processes. Our work has only addressed the significance of the CaMKK–CaMKIα cascade in GABA-mediated cortical axonogenesis during the perinatal period. Whether other GABA-regulated processes may also be mediated by CaMKIα clearly remains to be investigated. For instance, the process of cortical migration has also been reported to be regulated by GABA through signal transduction pathways involving Ca^{2+}, both *in vitro* (Behar et al., 1996, 1998, 2000) and *in vivo* (Heck et al., 2007). Interestingly, treatment with calmidazolium, an inhibitor of calmodulin, reduces the migration rate in cerebellar granule cells (Kumada and Komuro, 2004). Additional studies are needed to determine whether the CaMKK–CaMKIα cascade may play additional roles in such developmental processes as well.

A CaMKK–CaMKIα pathway may regulate fine-sculpting of cortical wiring

We here established the critical importance of an axonogenic GABA–CaMKK–CaMKIα pathway during early development *in vitro*. Moreover, this study indicated that CaMKIα regulated activity-dependent extension of terminal cortical axons *in vivo*. Interestingly, premature elimination of excitatory GABA action by forced expression of KCC2 in newly born cortical neurons dramatically perturbed the morphological maturation of the dendrites (Cancedda et al., 2007) or of the terminal callosal axon branches (H. Mizuno, T. Hirano, and Y. Tagawa, unpublished data). Our present findings thus uncover an unexpected role of the CaMKK–CaMKIα cascade as one key mechanism in GABA-driven activity-dependent regulation of cortical connectivity. More studies are needed to establish whether and how other Ca^{2+}-mobilizing signals (e.g., BDNF) may spatially and temporally interact and perhaps cooperate with such an axonogenic GABA–CaMKK–CaMKIα pathway. Finally, our data lend support to the existence of a perinatal time window of structural refinement, during which spontaneous Ca^{2+} signaling regulated by trophic factors, guidance signals, and ambient neurotransmitters, such as BDNF or GABA, critically fine-tunes cortical connectivity, perhaps even before the receipt of the earliest sensory cues.

References

Behar TN, Li YX, Tran HT, Ma W, Dunlap V, Scott C, Barker JL (1996) GABA stimulates chemotaxis and chemokinesis of embryonic cortical neurons via calcium-dependent mechanisms. J Neurosci 16:1808–1818.

Behar TN, Schaffner AE, Scott CA, O'Connell C, Barker JL (1998) Differential response of cortical plate and ventricular zone cells to GABA as a migration stimulus. J Neurosci 18:6378–6387.

Behar TN, Schaffner AE, Scott CA, Greene CL, Barker JL (2000) GABA receptor antagonists modulate postmitotic cell migration in slice cultures of embryonic rat cortex. Cereb Cortex 10:899–909.

Ben-Ari Y, Gaiarsa JL, Tyzio R, Khazipov R (2007) GABA: a pioneer transmitter that excites immature neurons and generates primitive oscillations. Physiol Rev 87:1215–1284.

Bito H, Takemoto-Kimura S (2003) Ca^{2+}/CREB/CBP-dependent gene regulation: a shared mechanism critical in long-term synaptic plasticity and neuronal survival. Cell Calcium 34:425–430.

Bito H, Deisseroth K, Tsien RW (1996) CREB phosphorylation and dephosphorylation: a Ca^{2+}- and stimulus duration-dependent switch for hippocampal gene expression. Cell 87:1203–1214.

Blaeser F, Sanders MJ, Truong N, Ko S, Wu LJ, Wozniak DF, Fanselow MS, Zhuo M, Chatila TA (2006) Long-term memory deficits in pavlovian fear conditioning in Ca^{2+}/calmodulin kinase kinase alpha-deficient mice. Mol Cell Biol 26:9105–9115.

Cancedda L, Fiumelli H, Chen K, Poo MM (2007) Excitatory GABA action is essential for morphological maturation of cortical neurons *in vivo*. J Neurosci 27:5224–5235.

Dickson BJ (2002) Molecular mechanisms of axon guidance. Science 298:1959–1964.

Furuyashiki T, Arakawa Y, Takemoto-Kimura S, Bito H, Narumiya S (2002) Multiple spatiotemporal modes of actin reorganization by NMDA receptors and voltage-gated Ca^{2+} channels. Proc Natl Acad Sci U S A 99:14458–14463.

Gomez TM, Zheng JQ (2006) The molecular basis for calcium-dependent axon pathfinding. Nat Rev Neurosci 7:115–125.

Heck N, Kilb W, Reiprich P, Kubota H, Furukawa T, Fukuda A, Luhmann HJ (2007) GABA-A receptors regulate neocortical neuronal migration in vitro and in vivo. Cereb Cortex 17:138–148.

Hook SS, Means AR (2001) Ca^{2+}/CaM-dependent kinases: from activation to function. Annu Rev Pharmacol Toxicol 41:471–505.

Hudmon A, Schulman H (2002) Neuronal Ca^{2+}/calmodulin-dependent protein kinase II: the role of structure and autoregulation in cellular function. Annu Rev Biochem 71:473–510.

Ishikawa Y, Tokumitsu H, Inuzuka H, Murata-Hori M, Hosoya H, Kobayashi R (2003) Identification and characterization of novel components of a Ca^{2+}/calmodulin-dependent protein kinase cascade in HeLa cells. FEBS Lett 550:57–63.

Kater SB, Mattson MP, Cohan C, Connor J (1988) Calcium regulation of the neuronal growth cone. Trends Neurosci 11:315–321.

Kumada T, Komuro H (2004) Completion of neuronal migration regulated by loss of Ca^{2+} transients. Proc Natl Acad Sci U S A 101:8479–8484.

Mizuno H, Hirano T, Tagawa Y (2007) Evidence for activity-dependent cortical wiring: formation of interhemispheric connections in neonatal mouse visual cortex requires projection neuron activity. J Neurosci 27:6760–6770.

Nairn AC, Greengard P (1987) Purification and characterization of Ca^{2+}/calmodulin-dependent protein kinase I from bovine brain. J Biol Chem 262:7273–7281.

Nonaka M, Doi T, Fujiyoshi Y, Takemoto-Kimura S, Bito H (2006) Essential contribution of the ligand-binding βB/βC loop of PDZ1 and PDZ2 in the regulation of postsynaptic clustering, scaffolding, and localization of postsynaptic density-95. J Neurosci 26:763–774.

Owens DF, Boyce LH, Davis MB, Kriegstein AR (1996) Excitatory GABA responses in embryonic and neonatal cortical slices demonstrated by gramicidin perforated-patch recordings and calcium imaging. J Neurosci 16:6414–6423.

Payne JA, Rivera C, Voipio J, Kaila K (2003) Cation-chloride co-transporters in neuronal communication, development and trauma. Trends Neurosci 26:199–206.

Represa A, Ben-Ari Y (2005) Trophic actions of GABA on neuronal development. Trends Neurosci 28:278–283.

Rivera C, Voipio J, Payne JA, Ruusuvuori E, Lahtinen H, Lamsa K, Pirvola U, Saarma M, Kaila K (1999) The K^+/Cl^- co-transporter KCC2 renders GABA hyperpolarizing during neuronal maturation. Nature 397:251–255.

Saneyoshi T, Wayman G, Fortin D, Davare M, Hoshi N, Nozaki N, Natsume T, Soderling TR (2008) Activity-dependent synaptogenesis: regulation by a CaM-kinase kinase/CaM-kinase I/betaPIX signaling complex. Neuron 57:94–107.

Schmitt JM, Wayman GA, Nozaki N, Soderling TR (2004) Calcium activation of ERK mediated by calmodulin kinase I. J Biol Chem 279:24064–24072.

Soderling TR (1999) The Ca-calmodulin-dependent protein kinase cascade. Trends Biochem Sci 24:232–236.

Soderling TR, Stull JT (2001) Structure and regulation of calcium/calmodulin-dependent protein kinases. Chem Rev 101:2341–2352.

Suzuki S, Numakawa T, Shimazu K, Koshimizu H, Hara T, Hatanaka H, Mei L, Lu B, Kojima M (2004) BDNF-induced recruitment of TrkB receptor into neuronal lipid rafts: roles in synaptic modulation. J Cell Biol 167:1205–1215.

Takemoto-Kimura S, Terai H, Takamoto M, Ohmae S, Kikumura S, Segi E, Arakawa Y, Furuyashiki T, Narumiya S, Bito H (2003) Molecular cloning and characterization of CLICK-III/CaMKIgamma, a novel membrane-anchored neuronal Ca^{2+}/calmodulin-dependent protein kinase (CaMK). J Biol Chem 278:18597–18605.

Takemoto-Kimura S, Ageta-Ishihara N, Nonaka M, Adachi-Morishima A, Mano T, Okamura M, Fujii H, Fuse T, Hoshino M, Suzuki S, Kojima M, Mishina M, Okuno H, Bito H (2007) Regulation of dendritogenesis via a lipid-raft-associated Ca^{2+}/calmodulin-dependent protein kinase CLICK-III/CaMKIgamma. Neuron 54:755–770.

Tessier-Lavigne M, Goodman CS (1996) The molecular biology of axon guidance. Science 274:1123–1133.

Tokumitsu H, Inuzuka H, Ishikawa Y, Ikeda M, Saji I, Kobayashi R (2002) STO-609, a specific inhibitor of the Ca^{2+}/calmodulin-dependent protein kinase kinase. J Biol Chem 277:15813–15818.

Tokumitsu H, Inuzuka H, Ishikawa Y, Kobayashi R (2003) A single amino acid difference between alpha and beta Ca^{2+}/calmodulin-dependent protein kinase kinase dictates sensitivity to the specific inhibitor, STO-609. J Biol Chem 278:10908–10913.

Tokumitsu H, Hatano N, Inuzuka H, Sueyoshi Y, Yokokura S, Ichimura T, Nozaki N, Kobayashi R (2005) Phosphorylation of Numb family proteins. Possible involvement of Ca^{2+}/calmodulin-dependent protein kinases. J Biol Chem 280:35108–35118.

Uboha NV, Flajolet M, Nairn AC, Picciotto MR (2007) A calcium- and calmodulin-dependent kinase Iα/microtubule affinity regulating kinase 2 signaling cascade mediates calcium-dependent neurite outgrowth. J Neurosci 27:4413–4423.

Uezu A, Fukunaga K, Kasahara J, Miyamoto E (2002) Activation of Ca^{2+}/calmodulin-dependent protein kinase I in cultured rat hippocampal neurons. J Neurochem 82:585–593.

Wang CL, Zhang L, Zhou Y, Zhou J, Yang XJ, Duan SM, Xiong ZQ, Ding YQ (2007) Activity-dependent development of callosal projections in the somatosensory cortex. J Neurosci 27:11334–11342.

Wang DD, Kriegstein AR (2008) GABA regulates excitatory synapse formation in the neocortex via NMDA receptor activation. J Neurosci 28:5547–5558.

Wayman GA, Kaech S, Grant WF, Davare M, Impey S, Tokumitsu H, Nozaki N, Banker G, Soderling TR (2004) Regulation of axonal extension and growth cone motility by calmodulin-dependent protein kinase I. J Neurosci 24:3786–3794.

Wayman GA, Impey S, Marks D, Saneyoshi T, Grant WF, Derkach V, Soderling TR (2006) Activity-dependent dendritic arborization mediated by CaM-kinase I activation and enhanced CREB-dependent transcription of Wnt-2. Neuron 50:897–909.

Yokokura H, Terada O, Naito Y, Hidaka H (1997) Isolation and comparison of rat cDNAs encoding Ca^{2+}/calmodulin-dependent protein kinase I isoforms. Biochim Biophys Acta 1338:8–12.

nature Vol 465|13 May 2010|doi:10.1038/nature09033

ARTICLES

Widespread transcription at neuronal activity-regulated enhancers

Tae-Kyung Kim[1]*†, Martin Hemberg[2]*, Jesse M. Gray[1]*, Allen M. Costa[1], Daniel M. Bear[1], Jing Wu[3], David A. Harmin[1,4], Mike Laptewicz[1], Kellie Barbara-Haley[5], Scott Kuersten[6], Eirene Markenscoff-Papadimitriou[1]†, Dietmar Kuhl[7], Haruhiko Bito[8], Paul F. Worley[3], Gabriel Kreiman[2] & Michael E. Greenberg[1]

We used genome-wide sequencing methods to study stimulus-dependent enhancer function in mouse cortical neurons. We identified ~12,000 neuronal activity-regulated enhancers that are bound by the general transcriptional co-activator CBP in an activity-dependent manner. A function of CBP at enhancers may be to recruit RNA polymerase II (RNAPII), as we also observed activity-regulated RNAPII binding to thousands of enhancers. Notably, RNAPII at enhancers transcribes bi-directionally a novel class of enhancer RNAs (eRNAs) within enhancer domains defined by the presence of histone H3 monomethylated at lysine 4. The level of eRNA expression at neuronal enhancers positively correlates with the level of messenger RNA synthesis at nearby genes, suggesting that eRNA synthesis occurs specifically at enhancers that are actively engaged in promoting mRNA synthesis. These findings reveal that a widespread mechanism of enhancer activation involves RNAPII binding and eRNA synthesis.

During development and in mature organisms, cells respond to changes in their environment in part through changes in gene expression. Extracellular factors including growth factors, hormones and neurotransmitters activate programs of new gene expression in a manner that is temporally and spatially controlled by the coordinated action of *trans*-acting transcription factors that bind to *cis*-acting DNA regulatory elements including enhancers, insulators and promoters. Most studies of the mechanisms by which gene expression is induced in response to extracellular stimuli have focused on promoters, which lie adjacent to the site at which mRNA synthesis is initiated. In contrast, the mechanisms by which enhancers[1], which lie far away from the start site of mRNA synthesis, contribute to stimulus-dependent gene expression are not well characterized. In the nervous system, hundreds of genes are induced in response to sensory experience-dependent neuronal activation[2]. Exposure of primary neuronal cultures to an elevated level of potassium chloride (KCl) leads to membrane depolarization and an influx of calcium through L-type voltage-sensitive calcium channels[2]. The resulting increase in intracellular calcium level then triggers several calcium-dependent signalling pathways that ultimately lead to changes in gene expression. We used this *in vitro* neuronal culture system to characterize neuronal activity-regulated enhancers.

Defining activity-regulated enhancers

Recent genome-wide studies have established that enhancers can be defined as DNA sequences that bind the transcriptional co-activator p300/CBP, that bind histone H3 monomethylated at lysine 4 (H3K4me1), and that are located distally from known transcription start sites (TSSs)[3–5]. We applied these criteria to define neuronal activity-regulated enhancers. Using ChIP-Seq[6], we first identified CBP binding sites throughout the mouse genome using two different antibodies against CBP and selected only those CBP-bound genomic loci detected by both antibodies (Methods). We found that CBP binding genome-wide is markedly increased upon membrane depolarization (Figs 1, 2, middle, and Supplementary Figs 1e, 2 and 3). Before stimulation, we detected fewer than 1,000 CBP binding sites, whereas upon membrane depolarization we detected ~28,000 CBP binding sites (Methods). Of the CBP sites detected upon membrane depolarization, ~25,000 were at least 1 kilobase (kb) distal to known TSSs, suggesting that most activity-dependent CBP binding does not occur at promoters. To identify specifically CBP binding sites at enhancers, we asked which of the distal CBP sites are also bound by H3K4me1-modified histones, which mark active chromatin regions including enhancers[3,7,8]. About 13,000 distal CBP sites are located within 2 kb of H3K4me1-modified regions (Figs 1, 2b and Supplementary Figs 1c and 3). We removed from this enhancer list a subset (7%) of enhancers that in addition to binding H3K4me1 also bind the transcription-initiation-site-associated histone mark H3K4me3 (refs 7, 8) and therefore may represent uncharacterized promoters (Figs 1, 2, top, and Supplementary Figs 1c, 3 and 8a). We defined the remaining ~12,000 genomic loci where distal CBP sites are flanked by H3K4me1 as neuronal enhancers (see Methods for detailed description of enhancer definition). Approximately half of the neuronal enhancers have evolutionarily conserved sequences in the region of CBP binding, indicating that these enhancers are functionally important (Fig. 1 and Supplementary Fig. 1a, b).

The strong inducibility of CBP binding at thousands of neuronal enhancers and their presence near activity-regulated genes (for

[1]Department of Neurobiology, Harvard Medical School, 220 Longwood Avenue, Boston, Massachusetts 02115, USA. [2]Department of Ophthalmology, Children's Hospital Boston, Center for Brain Science and Swartz Center for Theoretical Neuroscience, Harvard University, 300 Longwood Avenue, Boston, Massachusetts 02115, USA. [3]The Solomon H. Snyder Department of Neuroscience, Johns Hopkins University School of Medicine, 725 North Wolfe Street, Baltimore, Maryland 21205, USA. [4]Children's Hospital Informatics Program at the Harvard-MIT Division of Health Sciences and Technology, 300 Longwood Avenue, Boston, Massachusetts 02115, USA. [5]Molecular Genetics Core facility, Children's Hospital Boston, 300 Longwood Avenue, Boston, Massachusetts 02115, USA. [6]Epicentre Biotechnologies, 726 Post Road, Madison, Wisconsin 53713, USA. [7]Institute for Molecular and Cellular Cognition (IMCC), Center for Molecular Neurobiology (ZMNH), University Medical Center Hamburg-Eppendorf (UKE), Falkenried 94, 20251 Hamburg, Germany. [8]Department of Neurochemistry, Graduate School of Medicine, University of Tokyo, Bunkyo-ku, Tokyo 113-0033, Japan. †Present addresses: University of Texas Southwestern Medical Center, Department of Neuroscience, 5323 Harry Hines Blvd, Dallas, Texas 75390-9111, USA (T.-K.K.); Graduate Program in Neuroscience, University of California San Francisco, 1550 4th Street, San Francisco, California 94158, USA (E.M.-P.).
*These authors contributed equally to this work.

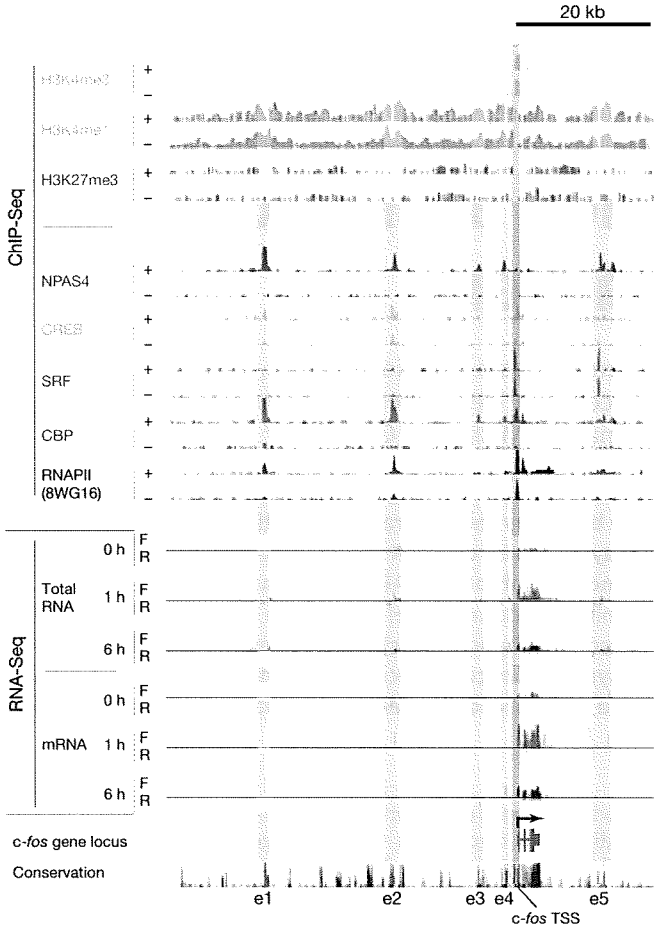

Figure 1 | Enhancers near the c-*fos* gene with increased CBP/RNAPII/NPAS4 binding and eRNA production upon membrane depolarization. ChIP-Seq: for each histone modification or transcription factor, two horizontal rows display the numbers of input-normalized ChIP-Seq reads across the locus, with '+' and '–' denoting the membrane-depolarized (2 h KCl) and unstimulated conditions, respectively. RNA-Seq: for each of 0, 1, or 6 h of membrane depolarization, the numbers of reads aligning to forward (F) and reverse (R) genomic strands are separately displayed. Enhancers identified in this study are highlighted by light-blue vertical bars (e1–e5), and the promoter region of c-*fos* gene is shown by a vertical light-red bar.

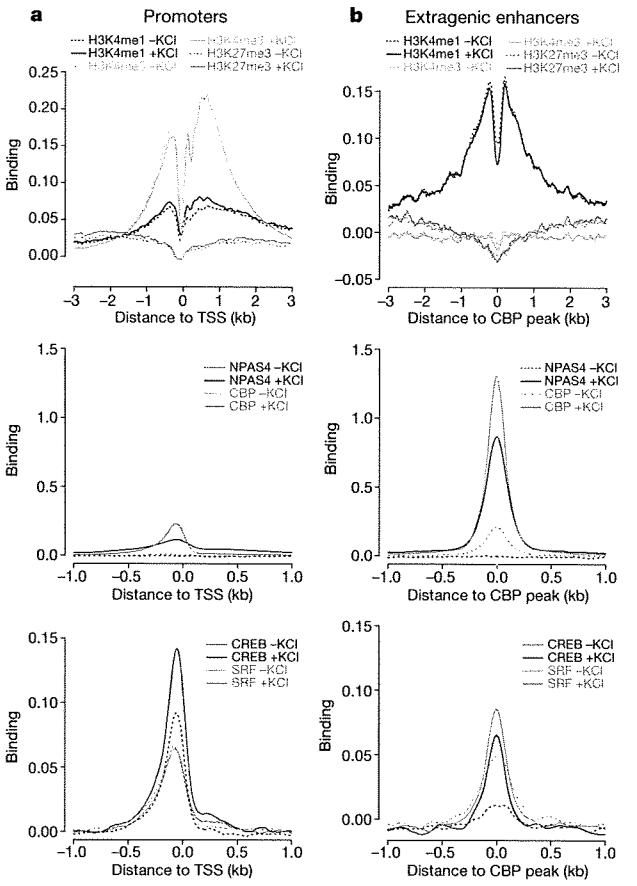

Figure 2 | Comparison of binding profiles between promoters and neuronal activity-regulated enhancers. a, b, Binding profiles of methylated histones and transcription factors at the promoter transcription start sites (TSSs) of 25,562 annotated genes (**a**) versus 5,117 extragenic enhancers (**b**). In each panel, binding profiles of methylated histones (top), CBP and NPAS4 (middle), and CREB and SRF (bottom) from unstimulated and membrane-depolarized (2 h KCl) neurons are shown. The *y* axes denote the degree of binding averaged across all promoters or enhancers, expressed as the mean number of input-normalized ChIP-Seq reads. Promoters are aligned at their annotated TSSs and enhancers are aligned at their CBP binding sites, with the *x* axes indicating the distance (kb) to either the TSS or the CBP peak.

example, c-*fos*, *Rgs2* and *Nr4a2*) (Figs 1, 2b, middle, and Supplementary Table 2) indicate that these enhancers may contribute to the induction of activity-regulated gene expression. One activity-regulated neuronal enhancer was independently identified as an enhancer that drives the activity-regulated transcription of *Arc* (also called *arg3.1*), a gene that regulates synaptic function[9–12]. This *Arc* enhancer, which is located 7 kb upstream of the *Arc* TSS, is necessary to drive activity-regulated *Arc* transcription[13,14]. To determine if the activity-regulated enhancers we identified have the ability to induce transcription at a promoter in an activity-dependent manner, we tested seven of the enhancers in a luciferase reporter assay (Fig. 3). We found that six out of seven enhancers were able to induce expression of luciferase in an activity-dependent manner. Consistent with the known properties of enhancers, the induction of luciferase expression required the presence of an intact promoter.

Characterization of enhancers

We next asked what properties of the enhancers in addition to CBP binding change dynamically when neurons are exposed to a stimulus that triggers activity-regulated gene transcription. H3K4me1 shows a bi-modal pattern of binding that spans a 2–4-kb region with CBP binding at its centre. We defined these H3K4me1-binding regions surrounding CBP binding sites as enhancer domains (Fig. 2b, top, and Supplementary Fig. 1c). The enhancer domains have very low levels of H3K4me3 and are devoid of H3K27me3, a histone marker that has been shown to be associated with either repressed or inactive genes (Fig. 2b, top). Furthermore, the levels of these histone marks are not significantly changed with membrane depolarization, suggesting that enhancer domains are maintained in an open chromatin conformation that is accessible for transcription factor binding, even in the absence of gene induction.

We asked whether transcription factors that are known to mediate activity-regulated gene expression bind to enhancers constitutively or in an activity-regulated manner. CREB, SRF and NPAS4 are known activity-regulated transcription factors that have an important role in various aspects of brain development including neuronal survival, synapse development and synaptic plasticity[15,16]. We find in neurons that CREB, SRF and NPAS4 bind to neuronal enhancers as well as promoters (Supplementary Table 3). Although both CREB and SRF bind enhancers before membrane depolarization, their binding at enhancers in some cases seems to be increased upon membrane depolarization (Fig. 2, bottom, and Supplementary Figs 1d, 2, 4a and 5). In contrast, the binding of NPAS4, which is not present in neurons at significant levels before membrane depolarization[16], was not detected before stimulation but was found at ~28,000

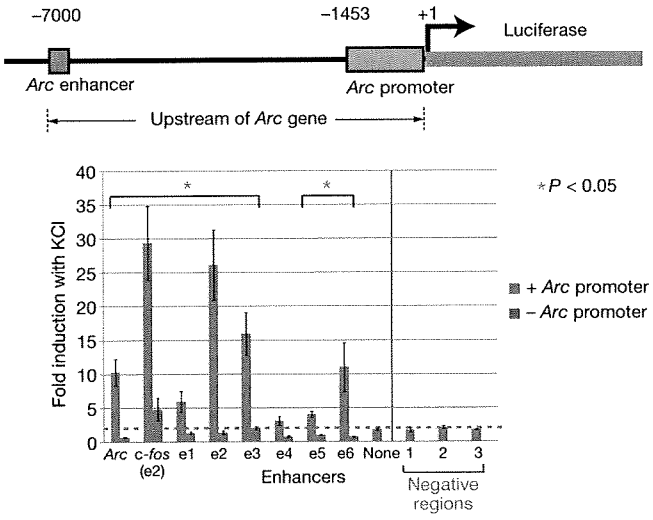

Figure 3 | Activity-induced luciferase expression mediated by neuronal enhancers. The *Arc* enhancer was replaced by six randomly chosen neuronal enhancers and one of the c-*fos* enhancers (e2; see Fig. 1) in the context of the ~7-kb region upstream of the *Arc* gene. The resulting fragments were placed upstream of a luciferase reporter gene, and activity-dependent expression of luciferase was measured in the presence or absence of the *Arc* proximal promoter after 6 h KCl treatment in rat cortical neurons. In additional control experiments, the *Arc* enhancer was removed, or three randomly chosen extragenic loci that do not show enhancer features were inserted. The red dotted line indicates the mean induction value of the three negative regions tested. Error bars indicate s.e.m. ($n = 3$ biological replicates); *P*-value from *t*-test.

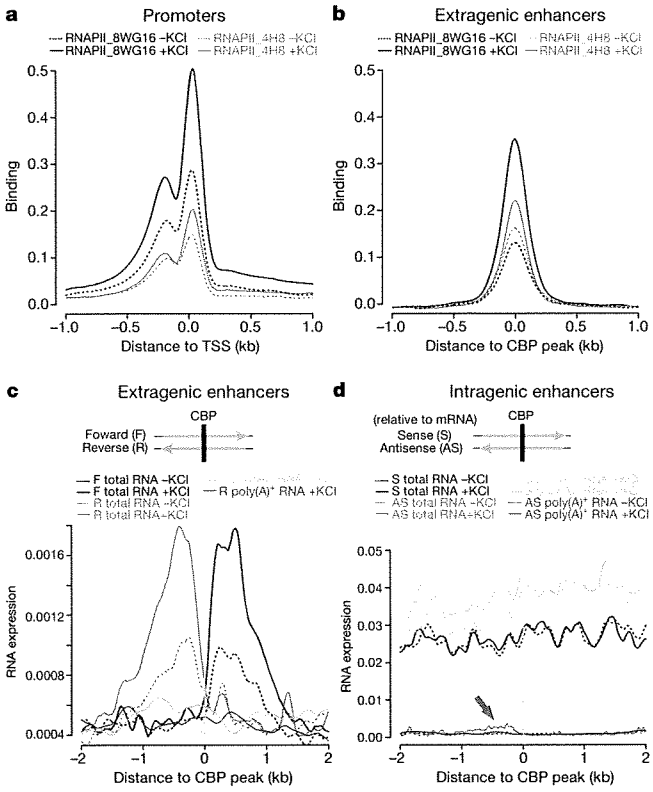

Figure 4 | Enhancers bind RNA polymerase II (RNAPII) and produce eRNAs. **a**, Binding profile of RNAPII at 25,562 TSSs of annotated genes using two different anti-RNAPII antibodies (8WG16 or 4H8). **b**, Binding profile of RNAPII at 5,117 extragenic enhancers. **c**, **d**, Profile of RNA expression at 5,117 extragenic enhancers (**c**) and at 6,718 intragenic enhancers (**d**) based on RNA sequencing of the total RNA and poly(A)$^+$ RNA fractions. The *y* axes report RNA expression as the normalized number of RNA-Seq reads per bp (Methods). In **c**, F and R denote forward (+) and reverse (−) genomic strands. In **d**, enhancers are aligned oriented relative to the gene in which they reside to allow for sense and antisense RNA-Seq reads to be shown separately. Although sense eRNAs cannot be detected due to overlapping mRNA transcription, the red arrow indicates a local increase in antisense RNA expression attributable to eRNAs (statistics in Methods). Note different scales on the *y* axis in **c** and **d**.

sites in membrane-depolarized neurons (Figs 1, 2, middle, and Supplementary Figs 1e, 2 and 3). NPAS4 binding was strongly biased towards enhancers relative to promoters, suggesting that NPAS4 may have a specific role in enhancer function (Supplementary Fig. 4a). Although we have shown that enhancer domains can be as long as 4 kb, our analysis of CREB, SRF, NPAS4 and CBP binding to enhancers indicates that these factors are predominantly located within 100 bp of the highly conserved centre of the enhancer domain (Supplementary Fig. 4b). This tight co-localization of individual transcription factors with CBP at a subset of enhancers (Supplementary Table 4) suggests that transcription factors may work together to regulate enhancer function, possibly by recruiting CBP.

Transcription at enhancers

At promoters, CBP recruits components of the basal transcription machinery, including RNAPII, thereby facilitating the assembly of functional transcription complexes that initiate mRNA synthesis[17]. Because CBP binds to enhancers in an activity-dependent manner, we asked if CBP also recruits RNAPII to these enhancers. To address this issue, we used ChIP-Seq to identify RNAPII binding sites across the genome using two different RNAPII antibodies. Consistent with previous studies[18,19], a large number of RNAPII sites were found to be located near annotated TSSs (Figs 1, 4a and Supplementary Fig. 4a). Notably, RNAPII also bound to ~3,000 activity-regulated enhancers (25%) (Figs 1, 4b and Supplementary Figs 1f, 3 and 4a), and the level of RNAPII binding was increased about twofold upon membrane depolarization (Fig. 4b and Supplementary Fig. 2). Although RNAPII has previously been reported to be present at several enhancers, including the β-globin and MHC class II gene enhancers[20,21], it has not been thought to have a widespread role in enhancer function. Given that CBP was previously known to recruit RNAPII to promoters and that increases in CBP and RNAPII binding coincide at thousands of enhancers in membrane depolarized neurons, it is likely that CBP has a role in the activity-regulated increase in RNAPII binding at enhancers. However, the observation that RNAPII is present at only a subset of CBP-bound enhancers suggests that additional activation steps beyond CBP binding may be required for RNAPII recruitment to enhancers.

The presence of RNAPII at enhancers raises the possibility that RNA transcription may occur at enhancers. Alternatively, the detection of RNAPII at enhancers might be an indirect consequence of the interaction of enhancers with active promoters, such that promoter-bound RNAPII gets crosslinked to enhancer DNA during the preparation of cells for ChIP-Seq experiments. To distinguish between these two possibilities, we used high-throughput RNA sequencing (RNA-Seq) to determine whether enhancer-bound RNAPII drives RNA synthesis at enhancers. Because it was not clear whether enhancer-derived transcripts would be polyadenylated, we sequenced total RNA, obtained from unstimulated or membrane-depolarized neurons after ribosomal RNA was depleted. To distinguish possible enhancer-derived transcripts from mRNA transcripts, we sought evidence of RNA transcription specifically at those ~5,000 activity-regulated enhancers located outside of annotated genes (extragenic enhancers). Surprisingly, we detected short (<2 kb) RNAs at ~2,000 extragenic enhancers (Figs 1, 4c, 5a, c and 6a). We observed dynamic changes in the levels of these enhancer RNAs (eRNAs) upon membrane depolarization, with a mean increase of ~2-fold (Fig. 4c). Synthesis of eRNAs seems to initiate near enhancer centres where CBP and RNAPII are bound and to proceed bi-directionally, extending to the

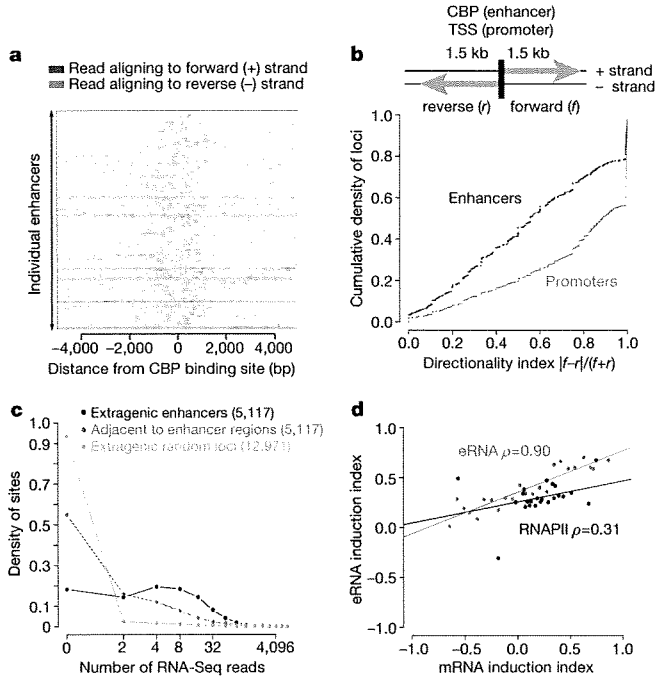

Figure 5 | eRNAs are transcribed bi-directionally, and their activity-dependent induction correlates with induction of nearby genes. a, RNA expression at 315 representative extragenic enhancers (see Methods for the enhancer selection and clustering). The enhancers are grouped into six categories using *k*-means clustering based on eRNA, RNAPII, CBP, NPAS4, CREB, SRF and H3K4me1 levels, with categories separated by horizontal black lines[3]. **b**, Directional bias of transcription initiated from enhancers and promoters, where *f* and *r* represent the numbers of reads (forward and reverse, respectively) aligning to the regions indicated (see Methods). **c**, The distribution of the number of RNA-Seq reads found within 1.5 kb of the extragenic enhancer loci, adjacent regions and random regions (see Methods). **d**, Changes in RNAPII binding and eRNA levels at extragenic enhancers versus changes in mRNA expression levels of nearby genes upon membrane depolarization. Each dot represents a set of genes that have similar mRNA induction indices and a corresponding set of enhancers nearby those genes (see Methods). The lines are the best linear fits to the points, and ρ is the Spearman correlation coefficient.

ends of the H3K4me1-modified enhancer domain (Figs 1, 4c, 5a, b, 6a and Supplementary Fig. 7a, b). Interestingly, we also detected eRNAs at ~1,000 of ~7,000 intragenic enhancers (Methods). Although high levels of mRNA transcription across intragenic enhancers prevented accurate quantification of eRNAs in the sense orientation, antisense eRNAs at intragenic enhancers were detectable and were similar in level to eRNAs at extragenic enhancers (Fig. 4c, d and Methods). These observations indicate that enhancers are not only sites where transcription factors bind and recruit RNAPII that might subsequently be delivered to promoters, but that enhancers are also sites where RNA synthesis occurs.

The strand-specific synthesis of eRNAs (Fig. 5a) and the dynamic changes in the level of eRNAs in response to neuronal activity suggest that the detection of eRNAs is not due to the sequencing of residual genomic DNA that is present in our purified RNA samples. Nevertheless, to confirm the existence of activity-regulated eRNAs at enhancers, we used an alternative method (DNaseI treatment followed by quantitative polymerase chain reaction with reverse transcription (RT–qPCR)) to detect these RNA transcripts (Supplementary Fig. 6). By RT–qPCR, we detected eRNAs at each of 18 enhancer loci tested. This result provides independent confirmation that the thousands of distinct eRNAs detected by RNA-Seq are bona fide RNA transcripts that are induced in an activity-dependent manner from neuronal enhancers.

We did not detect eRNAs in RNA-Seq from poly(A)$^+$ RNA fractions, suggesting that a large number of eRNAs may not be polyadenylated. Although it is possible that some polyadenylated eRNAs are present but not detectable at our current sequencing depth, two independent lines of evidence suggest that a large number of eRNAs may not be polyadenylated. First, using RT–qPCR, we observed that eRNAs were detected at higher levels in randomly primed reactions compared to oligo-dT-primed RT reactions (data not shown). Second, conventional sequencing of a circularized eRNA from the *Arc* enhancer confirmed that this transcript is not polyadenylated (Fig. 6). These experiments suggest that polyadenylation may not be a common feature of eRNA synthesis.

The detection of RNAPII binding and RNA synthesis at many enhancers could, in principle, result from mis-categorization of un-annotated promoters as enhancers. However, several lines of evidence suggest that both the extragenic and intragenic enhancers we have identified are indeed enhancers and are not un-annotated promoters. First, histone modification profiles at enhancers and annotated promoters are clearly distinguishable (Fig. 2, top, and Supplementary Figs 1c and 8a). Activity-regulated enhancers have high H3K4me1 and relatively low H3K4me3 levels, whereas promoters have lower H3K4me1 and high H3K4me3 levels. Second, the observation that eRNAs do not extend beyond the ~4-kb enhancer domain suggests that the eRNAs are much shorter (<2 kb for each strand) than transcripts initiated at most gene promoters (Figs 4c and 5a). Third, unlike promoters, enhancers do not produce detectable levels of polyadenylated RNA (Fig. 4c, d). Fourth, a promoter prediction algorithm (ProSOM)[22] revealed that fewer than 100 of ~12,000 enhancer regions are predicted to be promoters compared to 8,494 out of 27,854 annotated TSSs. Fifth, whereas sense transcription is more prevalent than antisense transcription at most promoters, transcription at enhancers seems to be less biased towards one particular strand (Fig. 5b). Finally, a few enhancers, including the well-characterized β-globin enhancer, have previously been shown to recruit RNAPII and drive transcription[23,24]. These findings argue against the possibility that RNAPII-bound enhancers that produce eRNAs are actually un-annotated promoters.

Mechanism of eRNA synthesis

Our observation that only a subset of the ~12,000 enhancers that inducibly bind CBP also bind RNAPII and drive eRNA transcription led us to hypothesize that RNAPII and/or eRNA synthesis might occur at a subset of enhancers that are actively engaged in promoting mRNA synthesis. To test this hypothesis, we investigated whether activity-regulated changes in RNAPII or eRNA levels at enhancers correlate with changes in mRNA levels at nearby genes (Fig. 5d and Supplementary Fig. 7c). The assumption in this analysis is that an enhancer is most likely to promote mRNA synthesis of the nearest gene[3,25]. We found that changes in eRNA expression levels that occur at enhancers upon membrane depolarization are strongly correlated with changes in mRNA expression levels at nearby genes. Changes in RNAPII levels at enhancers are also, to a lesser degree, correlated with changes in mRNA expression levels at nearby genes (Fig. 5d). Given that only a fraction of enhancers show inducible RNAPII binding or inducible eRNA synthesis, the binding of CBP to enhancers may not be sufficient for enhancer activation. Instead, enhancers exhibiting RNAPII binding and eRNA synthesis may represent a subset of CBP-bound enhancers that are actively engaged in promoting mRNA transcription.

The correlation between eRNA and mRNA induction suggests that eRNA synthesis may only occur when an enhancer interacts with the promoter of its target gene. In this scenario, eRNAs should not be generated from an enhancer when its target promoter is absent. We tested this hypothesis in the specific case of the mouse *Arc* enhancer using *Arc* knockout neurons in which most of the *Arc* gene, including the *Arc* promoter, is deleted but the *Arc* enhancer remains intact[10]. To characterize the *Arc* enhancer in *Arc* knockout neurons, we first performed chromatin immunoprecipitation (ChIP) experiments testing for the binding of SRF and RNAPII, two factors that we found

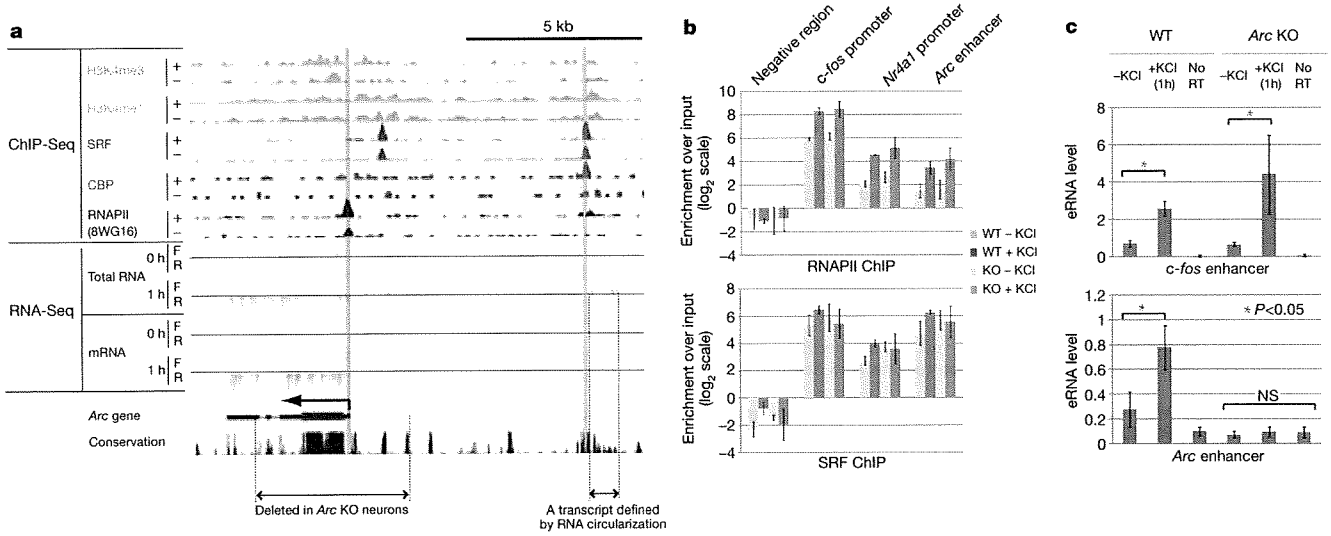

Figure 6 | eRNA synthesis but not RNAPII binding at the *Arc* enhancer requires the presence of the *Arc* promoter. a, The mouse *Arc* genomic locus with ChIP-Seq and RNA-Seq data as in Fig. 1. Also shown are the region deleted in the *Arc* knockout (*Arc* KO) mouse and a non-polyadenylated eRNA transcript defined by the RNA circularization method (Methods). **b**, Binding profiles of RNAPII and SRF at various loci determined by ChIP-qPCR from both wild-type and *Arc* knockout neurons. Error bars indicate s.e.m. ($n = 2$ biological replicates) **c**, RT–qPCR detection of the presence of eRNAs from wild-type and *Arc* knockout neurons. 'No RT' represents the qPCR signal from cDNA samples generated from reactions in which reverse transcriptase was omitted. Error bars are s.e.m. ($n = 3$ biological replicates); *P*-values are from *t*-test. NS, not significant.

by ChIP-Seq to be bound to the *Arc* enhancer (Fig. 6a, b)[13,14]. In *Arc* knockout neurons, both SRF and RNAPII remained bound at the *Arc* enhancer at levels equivalent to those observed in wild-type neurons, indicating that the binding of SRF and RNAPII to the *Arc* enhancer is independent of the *Arc* promoter. However, in the absence of the *Arc* promoter, we were not able to detect eRNA synthesis at the *Arc* enhancer (Fig. 6c). This absence of eRNA was specific to the *Arc* enhancer, as we observed robust induction of eRNA at a c-*fos* enhancer in the *Arc* knockout neurons. These results demonstrate that the recruitment of RNAPII to the *Arc* enhancer is not sufficient to drive eRNA synthesis and suggest that, like mRNA synthesis, eRNA synthesis may require an interaction of the enhancer with a promoter.

Discussion

We provide genome-wide evidence that thousands of neuronal activity-regulated enhancers that are defined by activity-independent H3K4me1 marks and activity-dependent CBP binding also recruit RNAPII and produce eRNAs. The observation of widespread RNAPII binding at enhancers suggests that a general mechanism of activity-dependent enhancer function in neurons may involve recruitment of RNAPII to enhancer loci, followed by subsequent transfer of RNAPII to promoters. Previous studies of a few individual enhancer loci have proposed several models for delivery of RNAPII from an enhancer to a promoter, including tracking of RNAPII along DNA and direct transfer of RNAPII via DNA looping[20]. Our observation that eRNAs are produced only within 2-kb enhancer domains and not along the entire distance between enhancers and promoters indicates that transcription-dependent RNAPII tracking is not likely to be a widespread mechanism of RNAPII delivery.

Our finding that large numbers of neuronal activity-regulated enhancers recruit RNAPII implies that enhancers may be more similar to promoters than previously appreciated. However, our analysis of the *Arc* enhancer in neurons lacking the *Arc* promoter demonstrates that the transcriptional machinery assembled at the *Arc* enhancer is not able to drive transcriptional initiation without the *Arc* promoter. This finding may explain why the level of eRNA synthesis is correlated with the level of transcription at the nearest promoter, and it suggests that eRNA synthesis at many enhancers may require a dynamic interaction between an enhancer and a promoter.

A remaining question is whether eRNAs have a specific biological function. In one model, the RNAPII-dependent transcriptional process at enhancers itself, rather than the eRNA transcripts it produces, may be important for enhancer function. For example, RNAPII has previously been shown to recruit chromatin-modifying enzymes such as histone methyltransferases[26]. In this regard, it is noteworthy that eRNAs are observed only within the H3K4me1-modified enhancer domain, and the level of the H3K4me1 modification and the level of eRNA synthesis are tightly correlated (compare Figs 2b, top, and 4c). Thus, the process of eRNA synthesis could be required to establish and maintain a chromatin landscape at enhancers that is required for enhancer function. However, it is also possible that the eRNA transcripts themselves are functionally important. The ability of enhancers to be transcribed in a regulated manner may provide an evolutionary mechanism by which new, functionally important genes or non-coding RNAs are generated.

METHODS SUMMARY

Directionality index at promoters and enhancers. A directionality index was defined as $|f - r|/(f + r)$, where f is the number of divergent reads on the forward strand and r is the number of divergent reads on the reverse strand within 1.5 kb of the CBP peak or TSS. (See Fig. 5b.)

Calculating the number of extragenic enhancers that produce eRNAs. The level of eRNA for each enhancer locus is calculated by counting all RNA-Seq reads found within a 1.5-kb region on both sides of the CBP peak. As a control, we consider the number of reads found in the adjacent regions (−3.5 kb to −2 kb) and (+2 kb to +3.5 kb) relative to the CBP peak, and in random regions. If one requires >7 reads for detection, 2,267 or 44% of the enhancers have eRNAs, compared to 16% of the flanking regions and 2% of the random regions. (See Fig. 5c.)

Changes in eRNA levels and RNAPII binding at enhancers. For changes in RNAPII binding at enhancers, we counted the number of ChIP-Seq reads within 300 bp of the enhancer centre at each time point. For eRNAs, we used the same procedure, including all reads within 1.5 kb of the enhancer. We defined the normalized induction index as $(s - u)/(s + u)$, where s and u are the number of normalized reads from the stimulated and unstimulated conditions, respectively. (See Fig. 5d.)

Correlations between enhancer features and mRNA expression levels at nearby genes. We paired each enhancer with the nearest TSS, provided that the distance was <1 Mb. The induction index for RefSeq genes was calculated as before for RNAPII, but based on the average read density throughout the coding region for mRNA. Genes were grouped by induction ratio quantiles into 25 bins before plotting. (See Fig. 5d.)

Full Methods and any associated references are available in the online version of the paper at www.nature.com/nature.

Received 21 October 2009; accepted 25 March 2010.
Published online 14 April 2010.

1. Banerji, J., Rusconi, S. & Schaffner, W. Expression of a β-globin gene is enhanced by remote SV40 DNA sequences. *Cell* **27**, 299–308 (1981).
2. Greer, P. L. & Greenberg, M. E. From synapse to nucleus: calcium-dependent gene transcription in the control of synapse development and function. *Neuron* **59**, 846–860 (2008).
3. Heintzman, N. D. *et al.* Distinct and predictive chromatin signatures of transcriptional promoters and enhancers in the human genome. *Nature Genet.* **39**, 311–318 (2007).
4. Visel, A. *et al.* ChIP-seq accurately predicts tissue-specific activity of enhancers. *Nature* **457**, 854–858 (2009).
5. Xi, H. *et al.* Identification and characterization of cell type-specific and ubiquitous chromatin regulatory structures in the human genome. *PLoS Genet.* **3**, e136 (2007).
6. Park, P. J. ChIP-seq: advantages and challenges of a maturing technology. *Nature Rev. Genet.* **10**, 669–680 (2009).
7. Barski, A. *et al.* High-resolution profiling of histone methylations in the human genome. *Cell* **129**, 823–837 (2007).
8. Robertson, A. G. *et al.* Genome-wide relationship between histone H3 lysine 4 mono- and tri-methylation and transcription factor binding. *Genome Res.* **18**, 1906–1917 (2008).
9. Chowdhury, S. *et al.* Arc/Arg3.1 interacts with the endocytic machinery to regulate AMPA receptor trafficking. *Neuron* **52**, 445–459 (2006).
10. Plath, N. *et al.* Arc/Arg3.1 is essential for the consolidation of synaptic plasticity and memories. *Neuron* **52**, 437–444 (2006).
11. Shepherd, J. D. *et al.* Arc/Arg3.1 mediates homeostatic synaptic scaling of AMPA receptors. *Neuron* **52**, 475–484 (2006).
12. Waltereit, R. *et al.* Arg3.1/Arc mRNA induction by Ca^{2+} and cAMP requires protein kinase A and mitogen-activated protein kinase/extracellular regulated kinase activation. *J. Neurosci.* **21**, 5484–5493 (2001).
13. Kawashima, T. *et al.* Synaptic activity-responsive element in the Arc/Arg3.1 promoter essential for synapse-to-nucleus signaling in activated neurons. *Proc. Natl Acad. Sci. USA* **106**, 316–321 (2009).
14. Pintchovski, S. A., Peebles, C. L., Kim, H. J., Verdin, E. & Finkbeiner, S. The serum response factor and a putative novel transcription factor regulate expression of the immediate-early gene Arc/Arg3.1 in neurons. *J. Neurosci.* **29**, 1525–1537 (2009).
15. Flavell, S. W. & Greenberg, M. E. Signaling mechanisms linking neuronal activity to gene expression and plasticity of the nervous system. *Annu. Rev. Neurosci.* **31**, 563–590 (2008).
16. Lin, Y. *et al.* Activity-dependent regulation of inhibitory synapse development by Npas4. *Nature* **455**, 1198–1204 (2008).
17. Kee, B. L., Arias, J. & Montminy, M. R. Adaptor-mediated recruitment of RNA polymerase II to a signal-dependent activator. *J. Biol. Chem.* **271**, 2373–2375 (1996).
18. Brodsky, A. S. *et al.* Genomic mapping of RNA polymerase II reveals sites of co-transcriptional regulation in human cells. *Genome Biol.* **6**, R64 (2005).
19. Kim, T. H. *et al.* A high-resolution map of active promoters in the human genome. *Nature* **436**, 876–880 (2005).
20. Koch, F., Jourquin, F., Ferrier, P. & Andrau, J. C. Genome-wide RNA polymerase II: not genes only! *Trends Biochem. Sci.* **33**, 265–273 (2008).
21. Szutorisz, H., Dillon, N. & Tora, L. The role of enhancers as centres for general transcription factor recruitment. *Trends Biochem. Sci.* **30**, 593–599 (2005).
22. Abeel, T., Saeys, Y., Rouze, P. & Van de Peer, Y. ProSOM: core promoter prediction based on unsupervised clustering of DNA physical profiles. *Bioinformatics* **24**, i24–i31 (2008).
23. Ling, J. *et al.* HS2 enhancer function is blocked by a transcriptional terminator inserted between the enhancer and the promoter. *J. Biol. Chem.* **279**, 51704–51713 (2004).
24. Zhao, H. & Dean, A. An insulator blocks spreading of histone acetylation and interferes with RNA polymerase II transfer between an enhancer and gene. *Nucleic Acids Res.* **32**, 4903–4919 (2004).
25. Heintzman, N. D. *et al.* Histone modifications at human enhancers reflect global cell-type-specific gene expression. *Nature* **459**, 108–112 (2009).
26. Gerber, M. & Shilatifard, A. Transcriptional elongation by RNA polymerase II and histone methylation. *J. Biol. Chem.* **278**, 26303–26306 (2003).

Supplementary Information is linked to the online version of the paper at www.nature.com/nature.

Acknowledgements We thank members of the Greenberg laboratory for discussions and for critical reading of the manuscript. We thank S. Vasquez for preparing dissociated mouse cortical neurons. We thank L. Hu for generating antibodies. We thank the Molecular Genetics Core Facility at Children's Hospital Boston, including H. Schneider and S. Burgess, for operation of their SOLiD 3.0 sequencer (I.D.D.R.C). We thank the support and R&D teams at Life Technologies including S. Ranade, R. David, J. Ni, C. Barbacioru, M. Barker, G. Costa and K. McKernan. M.E.G. acknowledges the support of the Nancy Lurie Marks Family Foundation. We thank M. Dehoff for technical support in the *Arc* knockout experiments. This work was supported by the National Institutes of Health grants NS028829 (M.E.G.), R21EY019710 (G.K.), DP2OD006461 (G.K.) and MH-053608 (P.F.W.). This work was also supported by The Lefler postdoctoral fellowship (T-K.K.) and The Jane Coffin Childs Memorial Funds (T-K.K.), The Helen Hay Whitney postdoctoral fellowship (J.M.G.), The Children's Hospital Ophthalmology Foundation (G.K.), The Whitehall Foundation (G.K.), and The Klingenstein Fund (G.K.)

Author Contributions T-K.K., J.M.G. and M.E.G. conceived and designed experiments. T-K.K., J.M.G., M.H., G.K. and M.E.G. wrote the manuscript. T-K.K. optimized the protocol for ChIP-Seq library preparation to be suitable for the SOLiD sequencer and made all ChIP-Seq libraries used in this study. S.K. invented the library construction methodology used for all RNA sequencing reported here. J.M.G., A.M.C. and E.M.-P. made all RNA-Seq libraries. M.H., J.M.G. and D.A.H. performed bioinformatic analyses. K.B.-H. carried out the SOLiD bead preparation and sequencing. T-K.K., J.W., P.F.W. and A.M.C. performed the *Arc* knockout experiment. D.M.B. performed the luciferase experiments. M.L. performed the RNA circularization experiment. H.B. provided the pArc7000 plasmid. D.K. provided the *Arc* knockout mouse. All authors reviewed the manuscript.

Author Information Sequencing data have been submitted to the GEO repository under accession numbers GSE21161 (for all ChIP-Seq and RNA-Seq data) and HM047267 (for circularized *Arc* enhancer RNA). The bigWig files for genome browser visualization are posted online (see Supplementary Table 6). Reprints and permissions information is available at www.nature.com/reprints. The authors declare no competing financial interests. Correspondence and requests for materials should be addressed to M.E.G. (michael_greenberg@hms.harvard.edu).

METHODS

Mouse cortical cultures. E16.5 C57BL/6 mouse embryo cortices were dissected and then dissociated in 1× Hank's Balanced Salt Solution (HBSS), 20 mg ml^{-1} trypsin (Worthington Biochemicals), and 0.32 mg ml^{-1} L-cysteine (Sigma) for 10 min. Trypsin treatment was terminated with three 2-min washes in 1× HBSS with 10 mg ml^{-1} trypsin inhibitor (Sigma). Trituration of cells was performed with a flame-narrowed Pasteur pipette to dissociate cells fully. Neurons were seeded at an approximate density of 4×10^7 on 15-cm dishes. The dishes were pre-coated overnight with poly-ornithine (30 μg ml^{-1}, Sigma) in water, washed three times with water, and washed once with Neurobasal Medium (Life Technologies) before use. Neurons were maintained in 30 ml Neurobasal Medium containing B27 supplement (2%; Invitrogen), penicillin-streptomycin (50 μg ml^{-1} penicillin, 50 U ml^{-1} streptomycin, Sigma) and glutamine (1 mM, Sigma). Neurons were grown *in vitro* for 7 days. Eight millilitres of the medium was replaced with 10 ml fresh warm medium on the 4th and 6th days *in vitro*.

Membrane depolarization by applying extracellular potassium chloride (KCl). For KCl depolarization of neurons, days *in vitro* (DIV) 6 neurons were quieted overnight in 1 μM tetrodotoxin (TTX, Tocris) and 100 μM D(-)-2-amino-5-phosphonopentanoic acid (D-AP5, Tocris), and they were incubated for 0, 1, 2, or 6 h in 55 mM KCl. ChIP-Seq experiments made use of 0 or 2 h KCl treatment. RNA-Seq experiments were performed with 0, 1, or 6 h of KCl treatment. Luciferase assays were done at 6 h KCl.

Luciferase reporter assays. For testing enhancer functionality, we randomly selected seven extragenic enhancers and tested their ability to function as activity-regulated enhancers in a transfection assay in cultured rat cortical neurons. We transfected DIV 5 neurons using the calcium phosphate method. As a positive control, we used the pGL4.11-Arc7000-luc2P plasmid[27], hereafter referred to as pArc7000, consisting of 7 kb of sequence upstream of the *Arc* coding region. As a negative control, we used pGL4.11-Arc7000-del no 1.luc2P, hereafter referred to as pArc7000-del1, which lacks a 5′ ~250-bp fragment corresponding to the synaptic activity response element (SARE)[27] located 7 kb upstream of the *Arc* gene. To test candidate enhancers, we replaced the SARE (XhoI-SwaI) with ~1-kb fragments centred on the CBP peaks at candidate enhancers. For the negative control loci, we choose three genomic regions where we observed no factor binding (ChIP-Seq) and no RNA expression (RNA-Seq). To excise the *Arc* proximal promoter from each of the candidate enhancer plasmids, we cut with HindIII and re-circularized, which removes two HindIII fragments totalling 1.4 kb.

qPCR validation of eRNA expression and activity induction. For validating eRNA expression, we chose 18 eRNA transcripts that were detected within 1.5 kb of the CBP site. We isolated RNA from three biological replicate KCl experiments at 0, 1 and 6 h of KCl using Trizol (Invitrogen). Each RNA sample was treated with DNaseI (Invitrogen, amplification-grade DNaseI). After the treatment each RNA sample was brought to a volume of 300 μl by the addition of Nuclease Free Water (Ambion), and precipitated with Glycogen (Ambion 5 mg ml^{-1}, 1:100), 3 M NaOAc (Ambion, 1:10) and 2.5 volumes of 100% ethanol. Reverse transcription of the precipitated RNA was performed using the High Capacity cDNA synthesis kit (Applied Biosystems) with random priming. The cDNA was the source of input for quantitative PCR, using a Step One Plus Real-Time PCR Instrument and SYBR Green reagents (Applied Biosystems). Each primer set used in the analysis was validated using a standard curve obtained from serial dilutions of genomic DNA. Each primer set included in the analysis had melt curves that were consistent with the amplification of a single product in the expected size range. The detectability plot was constructed with concentration values normalized to genomic DNA in the case of eRNA primers, or dilutions of cDNA for gene primers. The inducibility plot was constructed using concentration values that were normalized to corresponding tubulin concentrations.

RNA isolation. RNA was isolated from cultures using 30 ml Trizol on each 15-cm culture dish according to the manufacturer's instructions (Life Technologies). Up to four dishes were solubilized using the same 30 ml Trizol for a yield of 500–1,000 μg total RNA.

To define the 5′ and 3′ termini of uncharacterized RNAs, we circularized RNA, reverse-transcribed circular RNAs using random priming, and PCR-amplified the ligation junctions for conventional sequencing. We generally followed the protocol from ref. 28 with exceptions noted below.

(1) Total RNA from 1-h KCl-treated neurons was first treated with DNaseI as follows: 100 μg of RNA was incubated with 100 units of DNaseI, Amplication Grade (Invitrogen) in 1 ml of the supplied 1× buffer. Then 100 μl of 25 mM EDTA was added and the DNaseI was deactivated at 75 °C for 10 min. RNA was extracted with phenol and chloroform and precipitated with ethanol.

(2) Next we decapped the DNaseI-treated RNA as follows: 10 μg of the RNA was incubated with 25 units of tobacco acid pyrophosphatase (that is, TAP) (Epicentre) in the provided 1× buffer at 37 °C for 1 h. RNA was extracted with phenol and chloroform and precipitated with ethanol.

(3) RNA was circularized using T4 DNA ligase as follows: 8 μg of RNA in 2 ml of 50 mM Tris-HCl (pH 7.6), 10 mM $MgCl_2$, 1 mM ATP, 5% PEG-8000 was incubated with 20 units of T4 RNA ligase (Invitrogen) for 18 h at 37 °C. The ligase was inactivated at 65 °C for 10 min. RNA was extracted with phenol and chloroform and precipitated with ethanol.

(4) Reverse transcription was performed as described with the following modifications: we synthesized cDNA using 1 μg of circularized RNA as a template for cDNA synthesis and random hexameric primers following the Superscipt III reverse transcriptase kit (Invitrogen) in 20 μl reactions.

(5) PCR amplification was performed using a nested PCR approach. Primers were designed to amplify across possible 5′–3′ junctions. First, primary reactions were as follows: 1 μl of cDNA was cycled with 1 μM of each primary primer (Arc_R2new: AGGGTACAAGTAAACAAATACCTGA and Arc_L9new: AGT TCTCTAGCTAAGGCAAGCA) in Power SYBR (Applied Biosystems) mix in a total of 20 μl. Reactions were cycled as follows: 95 °C for 10 min and 20 cycles of 95 °C for 15 s, 60 °C for 30 s and 72 °C for 3 min. Second, the primary PCR reaction was further amplified on a qPCR machine using nested primers as follows: 10 μl of the primary PCR was cycled with 1 μM of each nested primer (Arc_R1new: TTAAGAGTCACAAAGCCACCAAT, Arc_L10new: GTCTCTAC CATTGATGGATCTC) in a 2 ml Power SYBR reaction divided into multiple wells. Nested PCR was performed as follows: 95 °C for 10 min and 40 cycles of 95 °C for 15 s, 60 °C for 1 min. Product was purified using QIAQuick PCR purification columns and sequenced conventionally. The product was mapped to the eRNA region using the UCSC Genome Browser (BLAT).

The sequence of the transcript obtained from this method is: ArcE1 + strand transcript, GGAGAGGTGGGGACCAGAGTCCCTGGCTGGAGACTGGTGAC ATTGTCCCTGCCATTGGTGGCTTTGTGACTCTTAAACCAGACCTGCACA AAGATCTTGTATCAGGTATTTGTTTACTTGTACCCTAGAGCTCTGGTTC CAGGAGAAAGCAGATGGCCCCCCGGGTGGGGGGGCCCTGGGCAGTAG TAGCTCCTCAGTCCTGTAAATAAATCCCTAGGAACAGCGTTCAGGCTG AAGGGTTCGAGCTCTGGGCTGGGCGTACACCAGCGCCAAGATGCAGA CAGGTAAGAATGCTTAGAATTCCTGTGCCTGACATTTCTCATTCTGTCA CAAAGGGGAGTGGGGTACCAATAGGGATGGAGCACAGTGCCCTGAAA GAGTTCAGATTCACACAGAGAACCAGGAAGGGCTTCCTAGAGGTGGAG CCTGTGGGTAGAAGGCAAAGAGCACAGGTTGAGCAGGGGAGGCCAGT GCTGTGTCCCCTCCACTCTTTTGGCTCCCTAATGGCCTTCAAGCGTGG TTACCCTCCTCTGGCTGGTGACTCCTCCGTTTTCTCTCTGGGCGGGGA GGGTGTTGGATCTGGACCTCTTTCTTTCTCCGATGTCTCCTCCTACCAG AGGCAGCTCATCTGAGTTCTCAAGCCTTTGCCCTGGGCTTTGAAACTG ACAACCAGCTCCCAGTGAGTGACCTGTGGAGCTGCAGACATGTGGAGA TCCAAGTTGTCTCCCCACTTCCTGTAGTTCTCTAGCTAAGGCAAGCAG GTCTCTACCATTGATGGATCTCACAGGTACCAGGCACGACTCTCGGTC CCTCGACCCACTGGAAAAGGTTGTGCATGGGTTCAGGGT.

SOLiD sequencing. SOLiD sequencing of ChIP-Seq and RNA-Seq libraries were performed on a SOLiD instrument (1, 2, or 3.0 version) with 35-bp reads according to manufacturer's instructions (Life Technologies). All experiments were performed on full sequencing slides with barcodes used to distinguish up to 16 sequencing libraries on a slide. Libraries were quantified by SYBR green quantitative-PCR (qPCR) to determine appropriate mixing ratios, which also depended on the desired sequencing depth for each of the libraries in the mixture.

Chromatin immunoprecipitation sequencing (ChIP-Seq). Forty million mouse cortical neurons cultured to *in vitro* day 7 were used for each ChIP-Seq library construction. ChIP was performed as described[29] using antibodies listed above. The immunoprecipitated DNA fragments were repaired by the End-It DNA End Repair Kit (Epicentre Biotechnology) according to the manufacturer's instructions. The end-repaired ChIP DNA fragments were purified by MinElute Reaction Cleanup Kit (Qiagen) and eluted in 20 μl in EB buffer. The resulting DNA fragments were ligated with P1 and P2 adaptors for SOLiD genome analyser (adaptor sequences can be made available upon request) for 20 min at room temperature using the Quick Ligase Kit (NEB), followed by purification using the MinElute Reaction Cleanup Kit (Qiagen). The purified, adaptor-ligated ChIP DNA fragments were subject to 6% native-PAGE for an in-gel PCR reaction. A gel slice containing 175–200 bp adaptor-ligated ChIP DNA fragments (corresponding to 125–150 bp genomic fragment sizes) was cut and shredded. PCR Platinum Supermix (100–200 μl, Invitrogen), 50 pmol of PCR primers (available upon request), 0.5 μl Taq DNA polymerase (NEB), and 0.15 μl p.f.u. Turbo DNA polymerase (Stratagene) were added into the shredded gel slice. The adaptor-ligated ChIP DNA fragments were amplified by 15 cycles of in-Gel PCR. After the PCR reaction, gel pieces were filtered out by 0.45 μm filter spin column, and the amplified ChIP-Seq library was purified by the MinElute PCR purification kit (Qiagen). The library was purified by one more round of 6% PAGE. A gel slice containing 200–250 bp PCR products (110–150 bp fragment size) was cut and shredded, and the amplified library was extract out of the gel by passive elution in elution buffer (1.5 M ammonium acetate in 1× TE). Gel pieces were

filtered out by filter spin column, and the resulting ChIP-Seq library was purified using the Qiaquick PCR purification kit (Qiagen).

Whole-transcriptome sequencing (WT-Seq: sequencing of total RNA). WT-Seq was performed according to a protocol/kit now available from Life Technologies, with minor modifications that are included below. Briefly, 5–10 μg of RNA isolated from mouse cortical cultures was depleted of ribosomal RNAs using two rounds of Human/Mouse RiboMinus treatment (Life Technologies) with overnight ethanol precipitations for sample re-concentration. The removal of ribosomal RNAs was confirmed on a Bioanalyser Nano Chip (Agilent). A total of 500–1,000 ng of riboRNA-depleted total RNA was fragmented with 10–18 min at 37 °C RNaseIII treatment, and 10 min of RNaseIII inactivation at 65 °C. Fragmentation was followed by size selection of ~50 to ~150 bp fragments using the flashPAGE denaturing PAGE-fractionator (Life Technologies) and ethanol precipitation overnight. The resulting RNA was directionally ligated, reverse-transcribed and RNaseH treated.

After trial PCR to assess library quality and quantity, 30 μl cDNA was run on a native 6% PAGE gel. The 90–120-bp size window (corresponding to 50–80-bp RNA insert size) was cut from the gel, shredded and inserted directly into a 400 μl PCR reaction using standard WT-Seq kit components and submitted to 11–15 cycles of PCR. The PCR product was phenol-chloroform extracted, ethanol precipitated and re-suspended in 20 μl WT-Seq gel loading buffer. The resulting sample was run on a 6% native PAGE gel, and the 150–175-bp size range (corresponding to 60–85 bp) was cut from the gel, shredded, and extracted overnight in WT-Seq PAGE elution buffer. The resulting library was filtered through 0.45 μm spin filters (Life Technologies) to remove gel pieces and ethanol precipitated.

We note that WT-Seq can detect neither the 5′-most fragment from transcripts with 5′-modified ends (such as mRNA 5′ 7-methyl-guanosine caps) nor the 3′-most fragment from transcripts with 3′-modified ends. However, for transcripts long enough to produce multiple ≥50-bp fragments, WT-Seq should detect the remaining fragments.

Mouse cortical neuron WT-Seq data presented in this manuscript are from one specific biological replicate, but each result was confirmed in at least one additional replicate.

mRNA sequencing (mRNA-Seq). mRNA-Seq was performed exactly as WT-Seq, except that the ribosomal RNA-removal steps were replaced by two rounds of polyA purification using the FastTrack MAG mRNA isolation kit (Life Technologies). The removal of ribosomal RNAs was confirmed on a Bioanalyser Nano Chip (Agilent).

Annotation version and mRNA TSS collection. For filtering CBP peaks to remove TSSs, we used all TSSs from UCSC known genes, Ensembl genes and RefSeq genes. The NCBI reference sequence (RefSeq) collection of mouse gene annotation, version 37_1, was used for analysing TSSs for comparison with enhancers (for example, Fig. 2a). A subset of RefSeq genes has multiple annotated TSSs per gene, and we used for these analyses only the 5′-most TSSs from these genes. Thus, 25,562 TSSs were used instead of the full set of 27,854 RefSeq TSSs.

Read alignment (mapping sequencing reads to the genome and splice junctions). ChIP-Seq, WT-Seq and mRNA-Seq sequencing reads were aligned using the large genomes matching pipeline from Life Technologies with parameters –e 3 –t 35 –z 10. These parameters dictate that 0–3 colour-space mismatches are allowed, a 35-bp read is aligned, and after 10 hits on a given chromosome, the aligner no longer looks for further matches. ChIP-Seq reads were aligned to the mouse NCBI genome version 37. WT-Seq and mRNA-Seq reads were also aligned to mouse NCBI 37, but in their cases, the genome was expanded with addition of a pseudo-chromosome consisting of exon–exon splice junctions, although reads aligning to splice junctions were used solely to assess the strand specificity of WT-Seq (next section). Only reads aligning to a single genomic position with a tolerance of 0–3 colour-space mismatches were used for findings reported in this manuscript.

ChIP-Seq read-length extension. After ChIP-Seq reads were aligned, they were extended to 120 bp to match the length of the DNA fragments that were sequenced. We chose to extend to 120 bp based on experimental considerations (see ChIP-Seq procedure, above), but we also confirmed that this was a reasonable extension distance bioinformatically using the procedure introduced by ref. 30.

Peak finding from ChIP-Seq. Chromatin immunoprecipitation followed by high-throughput sequencing (ChIP-Seq) experiments produces a large number of short (~120 bp) DNA fragments which are enriched in the regions where the transcription factor of interest was bound to the DNA. The resulting profile of the mapped short sequence reads to the DNA shows which regions are enriched for the transcription factor in question. As an example of such a profile, consider Fig. 1. The next challenge is to determine which of the enriched regions ('peaks') are statistically significant at a given threshold and what regions correspond to genomic background. The background is given by sequencing the input genomic DNA fragments. Thus, a peak is defined as a region that contains significantly more reads from the ChIP experiment than from the input control. We first determined the false discovery rate by using a sliding window with a width of 240 bp for every 10 bp in the mouse genome. Owing to repetitive sequences, it is impossible to assign 35-bp reads uniquely to some regions[31,32]. Consequently, such regions are excluded from our analysis. For each window, we calculated the statistic $D = R - N$ where R is the number of reads from ChIP, and N is the number of reads from an input sample. By considering the marginal distributions of R and N, we note that they both can be well approximated by a Poisson distribution with parameters λ_R and λ_N, respectively. It follows that D is a Skellam distribution[33]:

$$\Pr(D=d) \approx \mathrm{Ske}(d;\lambda_R,\lambda_N) = e^{-(\lambda_R+\lambda_N)}\left(\frac{\lambda_R}{\lambda_N}\right)^{d/2} I_{|d|}\left(2\sqrt{\lambda_R\lambda_N}\right) \quad (1)$$

where $I_{|d|}(z)$ is the modified Bessel function of the first kind of order $|d|$. When comparing the number of reads in a given window from two different samples, care must be taken to correct for differences in the total amount of sequenced reads. The construction of the null distribution from equation (1) takes unequal numbers of reads in the two samples into account by shifting the mode of the distribution so that mode will be positive if there are more ChIP reads than input control reads and negative if there are more reads for the input control sample. To determine the number of reads required for a 240-bp window to be significant, we use the local false discovery rate (locFDR) framework[34]. Using this methodology, we assume that the density of D, $f(D)$, can be written as the mixture $f(D) = p_0 f_0(D) + p_1 f_1(D)$, where f_0 is the null density, f_1 is the density of windows corresponding to true peaks and $p_0 + p_1 = 1$ with $p_0 \geq 0.9$. The locFDR, FDR(d), is related to the more familiar FDR[35] through

$$\mathrm{FDR}(d) = E[\mathrm{locFDR}(d) | D \geq d] \quad (2)$$

where E is the expectation with respect to the mixture density f. Taking CBP as an example, with a fixed threshold $f_p = 0.01$ and empirically estimated $\lambda_R = 0.346$ and $\lambda_N = 0.419$, we find that the critical difference is $d_0 = 5$ fragments. Inserting the empirical distribution and the Skellam null distribution from equation (1), we find that the FDR is $\sim 3 \times 10^{-6}$. For the H3K4me1 peaks, the procedure described above was used, except that the window size was changed to 1,000 bp at increments of 100 bp. The motivation for using a larger window size is that histone modifications are typically much broader than transcription factor binding sites and using a larger window allows us to consider a signal from a larger genomic region and the process becomes less sensitive to noise. The parameters for the Skellam distribution were $\lambda_R = 11.88$ and $\lambda_N = 1.33$, and from equation (2) we estimate the FDR to be $\sim 2 \times 10^{-5}$.

Reproducibility. To verify that our findings are robust and reproducible, we sequenced at least one biological replicate of each ChIP-Seq and RNA-Seq experiment. The correlations of enrichment (ChIP-Seq) or read numbers (RNA-Seq) are high, except in cases (such as enhancers with few RNA-Seq reads) where sensitivity is poor. We present scatter plots of replicates in Supplementary Fig. 10. In the specific case of CBP, we had one ChIP-Seq experiment using the Millipore antibody and several others using an Abcam antibody. As is often the case in ChIP experiments, the quality of the two experiments varied, with the Millipore antibody performing much better in terms of the proportion of reads under peaks. The quality of the CBP peaks are important for subsequent analysis, both in terms of their number (higher numbers result in better statistical power in downstream analyses) and their quality (false positive CBP sites will reduce the apparent fractional number of enhancers with RNAPII binding and eRNA expression). Thus, we took extra care to select high-confidence CBP sites. First, we used our highest quality ChIP-Seq (using Millipore CBP antibody) to call 41,148 peaks. Of these, 4,567 were also called as peaks in several Abcam ChIP-Seq experiments. In addition, we found that the enrichment of reads from the Abcam ChIP-Seq at the remaining 36,601 loci was substantially above the levels seen at randomly chosen regions. Thus, to gain additional sensitivity in identifying replicated peaks, we set a 0.1 false discovery rate (FDR) based on the 90th percentile of CBP Abcam enrichment at random loci. 23,346 CBP Millipore peaks not called as peaks in the Abcam IP were nonetheless found to be above the 0.1 FDR (Supplementary Fig. 11a). Thus, our final set of validated CBP peaks is 4,567 + 23,457 = 28,024 (Supplementary Fig. 11b).

Alternative peak-finding method. Because the location of the CBP peaks is key to all further analyses for this paper, we validated the results using another peak-finding algorithm called Sissrs[36]. We assumed a fragment length of 120 bp and we used an FDR of 0.001, but other than that, the default settings were not changed. Sissrs reported 32,656 CBP peaks (CBP Millipore, 2 h KCl), and we found that 31,842 (97.5%) of those were located within 1 kb of the peaks detected using our method. Using a more stringent threshold of 100 bp, 83% of the Sissrs peaks were found near one of our peaks. For the unstimulated condition, Sissrs reported

8,980 peaks, significantly more than we found. Closer inspection reveals that all of our peaks were within 1 kb of a Sissrs peak and 78% were within 100 bp. All peaks discovered by both our method and Sissrs for the unstimulated condition show a high degree of induction (Supplementary Fig. 9), indicating that the degree of CBP binding before KCl stimulation is very low.

Normalization of ChIP-Seq and RNA-Seq read numbers. To compensate for differences in total sequencing read depth among samples, all ChIP-Seq read counts were first normalized to their equivalent numbers assuming 10 million total reads per sample. Next, the normalized number of reads in the IP was subtracted from the normalized number of reads in the input within a 240-bp scanning window, and the subtracted value was used for further analysis and plotting. We refer to these two procedures respectively as normalization and input-subtraction. A similar procedure was performed for RNA-Seq data, where read counts were normalized to their equivalent numbers assuming 50 million reads per sample, and the normalized values were used for further analysis and plotting. Because ChIP-Seq reads correspond to the ends of larger DNA fragments produced by sonication, we extended each ChIP-Seq read to 120 bp.

Selecting random control regions. To generate a set of random peaks matching the CBP peaks we did the following for each intragenic peak: (1) calculate the distance d to the TSS of the overlapping gene; (2) select a gene g at random; (3) place the new random region d base pairs downstream of the TSS of gene g; (4) if d is larger than the length of g then the random location is invalid, and we draw a new g.

For extragenic peaks the procedure is similar: (1) calculate the distance d to the nearest TSS (at position t); (2) select a gene g at random; (3) place the new random region at $t+d$; (4) ensure that the location is extragenic; if it is not, then we draw a new g.

When selecting random control regions for comparing the eRNA levels found at the putative enhancers, we wanted to control for the genomic location relative to TSSs as well as for the difficulty of mapping reads to repetitive regions. We defined m as the fraction of 35-mers in a given region that are unique to the mouse genome. For both extra- and intragenic, we also make sure that m is greater than 0.8 and we exclude the sites that do not fulfil this criterion.

Defining enhancers based on ChIP-Seq data. To locate enhancers, we started from the set of 41,148 CBP (Millipore) peaks located by our peak-finding algorithm. Supplementary Table 1 indicates the number of CBP peaks at each stage of this filtering. (We note that the analysis in the main text and main figures is primarily focused on the extragenic peaks.) To be considered as enhancers, individual CBP peaks had to meet the following criteria: (1) the CBP peak had to be replicated with the Abcam CBP antibody (see reproducibility section). (2) The CBP peak had to be at least 1 kb away from all annotated TSSs. (3) CBP peaks with abnormally high levels of both H3K4me1 and H3K4me3 enrichment in a 2-kb bin centred on the peak were also removed. There were 159 sites that were disallowed based on this criterion. When examined in the UCSC Genome browser, these sites showed unusually long (>500 bp) regions of very strong enrichment for multiple transcription factors, suggesting that they were not true binding sites. (4) On the basis of evidence from ESTs and other annotations, it is reasonable to suspect that some of the loci in our enhancer sites could correspond to true promoters. We wanted to take a conservative approach, and hence we removed all CBP peaks that have a 5′-sequenced EST from the UCSC Genome Browser spliced EST track that has a 5′ end within 2 kb of the CBP peak and that spans an annotated TSS. (5) We removed peaks that showed evidence of initiating long transcripts. We compared the regions −4 to −2 kb relative to the CBP peak with the region +2 to +4 kb on the forward strand. If the density in the downstream region was significantly higher than in the upstream region, we took this as evidence that a longer, possibly coding transcript was initiated at the loci. (6) An H3K4me1 peak had to be present within 2 kb in both replicates of stimulated H3K4me1. (7) The enrichment of H3K4me3 within a 2 kb window centred on the peak had to be less than 2 in both unstimulated and stimulated cells (Supplementary Fig. 8). (8) A very small number of CBP peaks (for example, those found near ribosomal RNA genes) had >10,000 RNA-Seq reads mapped within 1.5 kb. We removed these loci to simplify our analysis of RNA-Seq reads at enhancers.

Selection and clustering of enhancers. For each of the transcription factors CBP, CREB, NPAS4, SRF and RNAPII, the 1,000 enhancers with the highest levels of input-normalized ChIP-Seq reads within 200 bp of the enhancer centre were selected as well as the 1,000 enhancers with the highest levels of H3K4me1 within 1 kb. The enhancers were pooled and the ones without any divergent reads within 1.5 kb were removed. Subsequently, 315 enhancers were selected at random and ordered by row on the basis of k-means clustering performed in R, based on the transcription factors mentioned above, the amount of H3K4me1 and the amount of divergent RNA-Seq signal (Fig. 5a).

Directionality index. A directionality index used in Fig. 5b was defined as $|f-r|/(f+r)$, where f is the number of divergent reads on the forward strand and r is the number of divergent reads on the reverse strand within 1.5 kb of the CBP peak or TSS. The estimation of the directionality index is complicated by the fact that the number of reads found at enhancers is much smaller than the number of reads found at promoters. To make sure that the observed difference is not an artefact due to the lower levels of eRNAs, we down-sampled the number of reads at promoters to match the eRNA read numbers.

Detection of enhancers with eRNAs. As a negative control for the eRNAs, we compared with the adjacent regions −3.5 to −2 kb and +2 to +3.5 kb. A less stringent control is provided by the random control loci where we used the −1.5 to +1.5 kb regions. If one requires >7 reads for detection, 2,267 or 44% of the enhancers have eRNAs, compared to 16% of the flanking regions and 2% of the random regions (Fig. 5c).

For the intragenic enhancers, in examining eRNA transcription we were limited to considering the antisense strand. Using a similar strategy to that shown in Fig. 5c, we found that 22% of intragenic enhancers had more than four antisense reads within 1.5 kb of the CBP peak, whereas 14% of the enhancers had more than four antisense reads in the flanking regions.

Changes in eRNA levels and RNAPII binding at enhancers. For changes in RNAPII binding at enhancers, we counted the number of ChIP-Seq reads within 300 bp of the enhancer centre at each time point. For eRNAs, we used the same procedure, including all reads within 1.5 kb of the enhancer. We defined the normalized induction index as $(s-u)/(s+u)$, where s and u are the number of normalized reads from the stimulated and unstimulated conditions, respectively (Fig. 5d).

Correlations between enhancer features and mRNA expression levels at nearby genes. We paired each enhancer with the nearest TSS, provided that the distance was <1 Mb. The induction index for RefSeq genes was calculated as before for RNAPII, but based on the average read density throughout the coding region for mRNA. Genes were grouped by induction ratio quantiles into 25 bins before plotting (Fig. 5d).

Searching for known consensus motifs. For each enhancer and TSS where an NPAS4 peak was found we searched for perfect matches to the NPAS4 consensus motifs 'CACGC' and 'CACGTA'[37] on both strands in a 300-bp window centred around the CBP peak or the TSS. Surprisingly, at least one of the motifs was found in 66% of the promoter peaks but only in 27% of the peaks found at enhancers. The fraction of enhancers with the NPAS4 motifs is only marginally larger than the 22% found at TSSs lacking NPAS4 binding or the 14% found at random loci. Given the fact that there is no significant difference between the peak sizes found at enhancers and promoters (Supplementary Table 1), this result suggests that the mechanism of binding of NPAS4 to promoters and enhancers may differ, as has been observed for other factors.

Induced genes. We provide Supplementary Table 8, showing a list of KCl-regulated genes used for analysis in Fig. 5. The list was generated using our most deeply sequenced RNA-Seq experiment and filtered for fold-change and a z-score ensuring adequate read number. The list of genes is consistent with previous experiments published using array technologies[27,38], and is well correlated with replicate RNA-Seq experiments.

Gene ontology analysis using DAVID. To examine whether particular gene classes were enriched either for CREB binding at their promoters or for regulation by KCl, we took KCl-regulated (Supplementary Table 8) or CREB-bound genes and asked whether particular gene classes were enriched. The results obtained using the software DAVID[39,40] are in Supplementary Table 7 (CREB) and Supplementary Table 9 (KCl-regulated genes).

Additional bioinformatics. Analysis of aligned reads was performed with a combination of custom Perl, Java, R, and MATLAB scripts. Additional details are available upon request.

Note on plots. In the case of plots with RefSeq promoters aligned by their mRNA TSSs: in each case, promoters are aligned so that the positions +1 to +1,000 bp along the x axis correspond to the first 1 kb of each reference sequence annotated pre-mRNA, and the positions −1,000 to −1 bp consist of the first 1 kb upstream of each mRNA TSS. For plots with enhancers aligned at the centre of their CBP binding site, the same logic applies with the CBP peak centre substituting for the mRNA TSS. Owing to different sequencing depths, different scales are required in Figs 1 and 6a for displaying different ChIP results. For Fig. 1, the scales are H3K4me3 (0–1), H3K4me1 (0–1), H3K27me3 (0–1), SRF (0–3.5), CBP (0–3), CREB (0–2), NPAS4 (0–3), RNAPII (0–3), RNA-Seq (0–10), where the numbers in parentheses are normalized read counts. The corresponding numbers for Fig. 6a are H3K4me3 (0–0.5), H3K4me1 (0–2), SRF (0–7), CBP (0–1), RNAPII (0–1.8), RNA-Seq (0–10). Note that no input subtraction was performed for these plots. The conservation track shows 30-way Multiz alignment and conservation scores (PhastCons).

27. Kawashima, T. *et al.* Synaptic activity-responsive element in the Arc/Arg3.1 promoter essential for synapse-to-nucleus signaling in activated neurons. *Proc. Natl Acad. Sci. USA* 106, 316–321 (2009).